Precise Control of Soft Robots Amidst Uncertain Environmental Contacts and Forces

Xinjia Huang, Zihao Yuan, Xinyu Yang, and Guoying Gu, *Senior Member, IEEE*

***Abstract*—Recent studies have reported on the remarkable ability of bioinspired soft robots to exhibit dexterous and contact-friendly motions. However, for these robots with deformable bodies, it is extremely challenging to achieve precise and robust control when undergoing uncertain forces and contact in the environment. In this work, we take a first step to address this issue for slender pneumatic soft robots by proposing a comprehensive modeling and control framework. Our framework employs a fully parametrized model that accurately describes both robot configurations and distributed forces using Hermite interpolation. Leveraging this model, we further establish an estimation algorithm that can infer complete robot configurations and distributed external forces from limited motion data, enabling perception of contact locations and forces. Integrating this model and estimator, our control framework achieves precise robot motion control under diverse forces, with the average trajectory tracking error within 0.3 mm. It also detects and adapts to uncertain contact, demonstrated in tests of automatic obstacle avoidance and precise grasping. This framework holds promise for various applications such as environmental exploration and safe manipulation, where compliant interaction with the environment is required.**

***Index Terms*—Environmental contact, force estimation, physics-based modeling, soft robotics.**

I. Introduction

SOFT robots possess a key advantage over rigid robots in that they can undergo compliant deformation upon contacting with their environment. This unique characteristic endows soft robots with improved safety in human–robot interaction, adaptability to diverse environments, and operational robustness [1], [2], [3], making them highly promising in the fields such as healthcare [4], [5], [6], compliant grasping [7], [8], [9], and environmental exploration [10], [11]. However, the use of compliant materials brings infinite passive degrees of freedoms leading to the challenges of precise modeling and control, especially with random payloads and unconstructive environments.

To address this challenge, extensive research efforts have been dedicated to developing model-based control strategies for soft robots. Among these works, the static and dynamic behaviors of soft robots have been characterized by a range of modeling techniques including physical methods such as spatial rod theories [12], [13], [14], [15], finite element methods [16], [17], [18], [19], and lumped system modeling [20], [21], as well as data-driven methods such as recurrent neural networks [22], [23], Koopman operator theory [24], [25], and Gaussian process regression [26]. Subsequently, the established models provide a foundation for implementing different control algorithms such as model predictive control [24], [27], feedback-linearization [28], [29], [30], and reinforcement learning [18], [31] across various soft robotic systems.

Nevertheless, the existing works mainly focus on the control of soft robots in free or predefined spaces. Unfortunately, achieving precise motion control for soft robots amidst uncertain contact and varying loads remains an unresolved challenge. This issue holds significant importance as the compliance advantage of soft robots only show during interactions with their environment. However, when these robots deform under uncertain contact conditions, achieving precise motion control becomes exceedingly difficult. The primary obstacles here include: i) perception of comprehensive interaction states between the soft robot and its environment—encompassing contact location and interaction forces—despite limited sensory input; ii) translating this perceived information into a control strategy adaptable to unknown working conditions, such as uncertain obstacles, manipulated objects, and diverse distributed payloads.

For the perception system, various types of external (e.g., vision [32], [33]) and embedded sensing techniques (such as soft strain sensors [34], [35], optical fiber sensors [36], and liquid metal sensors [37], [38]) have been applied to measure the motion states of soft robots. However, the comprehensive force sensing is still difficult. Though some soft tactile sensors have been integrated to soft robotic systems to detect external forces [39], [40], [41], the density of sensory units and measurement accuracy are usually limited by the crosstalk noise of electromagnetic signals and manufacture difficulties. More importantly, most of the current soft tactile sensors can only measure the force component perpendicular to the contact surface rather than the complete 3-D force vector.

In contrast to direct force sensing, some other works indicate the feasibility to estimate the forces acted on the soft robot by

Manuscript received 29 February 2024; revised 6 May 2024; accepted 18 June 2024. Date of publication 15 July 2024; date of current version 1 August 2024. This work was supported in part by the National Natural Science Foundation of China under Grant 52025057 and Grant T2293725, in part by the Science and Technology Commission of Shanghai Municipality under Grant 22511101700 and in part by the State Key Laboratory of Mechanical System and Vibration under Grant.MSVZD202301. This article was recommended for publication by Associate Editor H. Zhao and Editor A. Menciassi upon evaluation of the reviewers' comments.*(Corresponding author: Guoying Gu.)*

The authors are with the Institute of Robotics, State Key Laboratory of Mechanical System and Vibration, School of Mechanical Engineering, Shanghai Jiao Tong University, Shanghai 200240, China (e-mail: huangxinjia@sjtu.edu.cn; yuanzihao@sjtu.edu.cn; xinweiyujing@sjtu.edu.cn; guguoying@sjtu.edu.cn).

This article has supplementary downloadable material available at https://doi.org/10.1109/TRO.2024.3427339, provided by the authors.

Digital Object Identifier 10.1109/TRO.2024.3427339

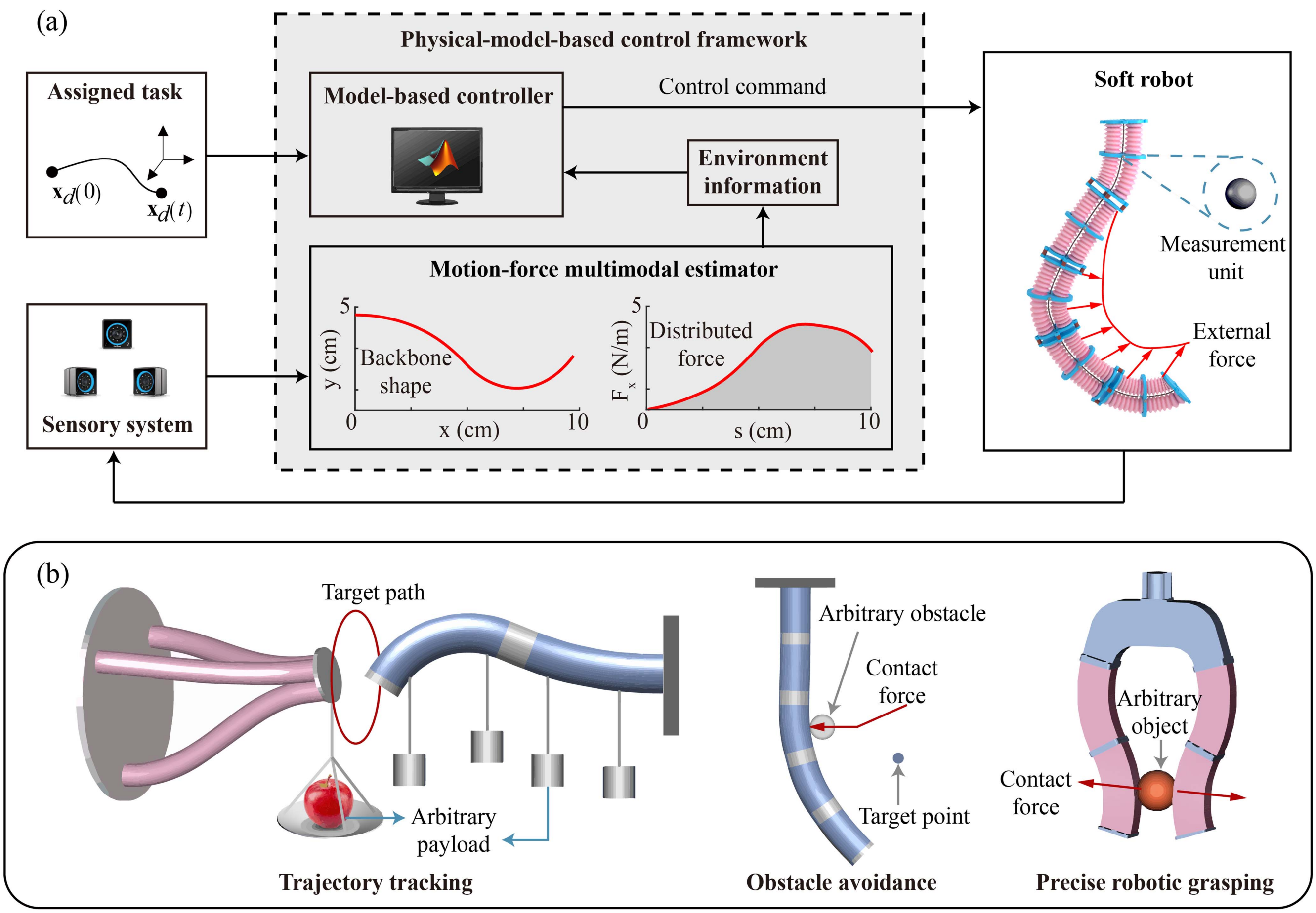

Fig. 1. Outline of this work. (a) Schematic illustration of a physics-model-based control framework for soft robots, integrated by a motion-force multimodal estimator and a feedback controller with real-time parameter update. (b) Proposed method enables soft robot performing various tasks with automatic response to uncertain working conditions, such as precise tracking control with arbitrary external payloads, automatic obstacle avoidance in unstructured environments, and precise robotic grasping of arbitrary objects.

measuring the motions or deformations [42], [43], [44], [45]. These works harness the inherent mechanical relation between the external forces and the motions of soft robots, which can be computed with a physical or data-driven model. Therefore, the difficulty in integrating stable force sensing system can be avoided by pure motion perception. However, existing force estimation algorithms often face limitations—some are computationally intensive for real-time implementation, while others are constrained to simplified scenarios involving concentrated payloads. These limitations may hinder their practical application in real-time control under uncertain contact conditions.

To the best of our knowledge, there is no existing work that has employed comprehensive motion-force perception to controller designs for soft robots under uncertain contact with the environment and varying distributed loads. In this study, we take a first step to address this issue by developing a new physical-model-based control framework of soft robots [see Fig. 1(a)], enabling adaptive responses to uncertain payloads, obstacles, and interacting objects [see Fig. 1(b)]. The essence of this framework lies in the establishment of a physical model that accurately parameterizes both the continuum motion states and continuously distributed external forces. Based on this model, we develop a multimodal estimator for soft robots that can compute the real-time continuum kinematic configurations and the distributions of external forces using limited motion sensing units. The combination of this estimator with model-based controllers enables precise motion control of soft robots in the presence of various uncertain working conditions. Specially, the developed estimator facilitates the recognition of obstacles in the environment and interacting objects, leading to intelligent applications such as autonomous obstacle avoidance with a soft manipulator and adaptive precise grasping with a soft robotic gripper. Thus, the proposed framework provides a foundation for empowering soft robots to exhibit intelligent behavior and interact effectively with their surrounding environments.

In summary, the main contributions of this work can be emphasized as follows:

i) A fully parameterized physical model of soft robots. Unlike other parameterized models purely focusing on describing the continuum robot configurations, we present a unified Hermite interpolation-based method to represent both the continuously distributed external forces and robot configurations simultaneously with finite parameters.

ii) A motion-force multimodal estimation algorithm. With this developed algorithm, the infinite-DOF robot configurations and continuously distributed external forces can be both estimated with finite sensing data in real time. Therefore, the interaction states between the soft robot and the environment (including the location of contact and interaction forces) can be efficiently detected.

iii) Model-based controllers integrated with the developed multimodal estimator. The designed controllers make the soft robot robust against randomly distributed payloads, obstacles, and interacting objects, which are verified by the tests of trajectory tracking, automatic obstacle avoidance, and precise grasping. By our introduction for the concept of virtual payloads, these controllers can work well even with nonnegligible modeling errors.

The rest of this article is organized as follows: In Section II, the fully parameterized physical model is presented. Based on this model, in Section III, we develop and verify a motion-force multimodal estimation algorithm. In Section IV, we integrate the multimodal estimator to controller designs for soft robots experiencing randomly distributed payloads. In Sections V and VI, we extend our developments for the tasks of autonomous obstacle avoidance and precise robotic grasping, respectively. Finally, Section VII concludes this article.

II. Parametric Modeling of Soft Robots

For soft robots, both the external forces (including the gravity) and the material deformation are distributed in their 3-D soft structures, which can be represented by a set of continuous functions of spatial material coordinates. Besides, polynomial interpolation is commonly used to approximate continuous functions by using the function values at defined nodes. Among the polynomial interpolation approaches, Hermite interpolation uses both function values and their derivatives to construct interpolating polynomials achieving better continuity and approximation to the original functions. Utilizing this technique to parameterize the continuous displacement field of flexible or soft structure, the method named absolute nodal coordinate formulation (ANCF) [46] has been applied for the kinematic modeling of soft robots [47], [48], [49]. However, in these ANCF-based models, only the continuum robot configurations are parametrically described, which is not enough for the analysis and estimation of continuously distributed external forces. In this work, we first utilize Hermite interpolation to map a finite-dimensional parameter vector $\mathbf{F}$ to the distributed forces, which is integrated with the ANCF-based motion parameterization. Then, we develop a fully parametrized model of soft robots where both the continuum robot configurations and continuously distributed external forces are completely described. In the following, we will present how this is achieved.

As illustrated in Fig. 2, we first discretize the soft robot into a set of elements along its backbone, where each element has two nodes defined at the both ends. Then, a local material coordinate system *O-XYZ* is defined for each element to label the material particles, where X is the axial coordinate, and Y and Z are coordinates perpendicular to it. Hence, the fields

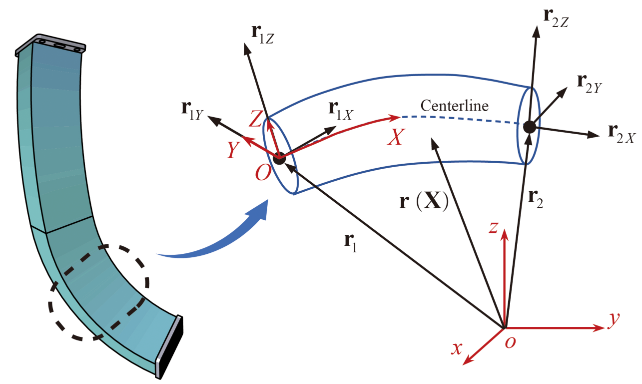

Fig. 2. Schematic diagram of the discretization for the soft robot.

of both displacements and external forces can be represented by vector-valued functions in the form as $\mathbf{f}(\mathbf{X}) \in \mathbb{R}^3$, where $\mathbf{X} \in \mathbb{R}^3$ is the material coordinate defined in the system *O-XYZ*. To approximately describe such functions by finite parameters, we assume the expression of $\mathbf{f}(\mathbf{X})$ as the following polynomials:

$$\mathbf{f}(\mathbf{X}) = \begin{bmatrix} \sum_{i=1}^{4} a_i X^{i-1} + a_5 Y + a_6 Z + a_7 XY + a_8 XZ \\ \sum_{i=1}^{4} b_i X^{i-1} + b_5 Y + b_6 Z + b_7 XY + b_8 XZ \\ \sum_{i=1}^{4} c_i X^{i-1} + c_5 Y + c_6 Z + c_7 XY + c_8 XZ \end{bmatrix} \tag{1}$$

where a_i, b_i, and c_i are polynomial coefficients. The function values and their gradients of $\mathbf{f}(\mathbf{X})$ at the both nodes are denoted as $\mathbf{f}_i \in \mathbb{R}^3\,(i = 1, 2)$ and $\mathbf{f}_{iL} = \partial \mathbf{f}/\partial L\,(i = 1, 2, L = X, Y, Z)$, respectively. For one element, if the values of $\mathbf{f}_i$ and $\mathbf{f}_{iL}$ are given, the polynomial coefficients in (1) can be obtained as

$$\begin{aligned}
&\begin{bmatrix} a_1 & b_1 & c_1 \end{bmatrix} = {\mathbf{f}_1}^T,\ \begin{bmatrix} a_2 & b_2 & c_2 \end{bmatrix} = {\mathbf{f}_{1X}}^T \\
&\begin{bmatrix} a_3 & b_3 & c_3 \end{bmatrix} = -\frac{{\mathbf{f}_{2X}}^T + 2{\mathbf{f}_{1X}}^T}{L_e} + \frac{3(\mathbf{f}_2 - \mathbf{f}_1)^T}{{L_e}^2} \\
&\begin{bmatrix} a_4 & b_4 & c_4 \end{bmatrix} = \frac{{\mathbf{f}_{2X}}^T + {\mathbf{f}_{1X}}^T}{{L_e}^2} + \frac{2(\mathbf{f}_1 - \mathbf{f}_2)^T}{{L_e}^3} \\
&\begin{bmatrix} a_5 & b_5 & c_5 \end{bmatrix} = {\mathbf{f}_{1Y}}^T,\ \begin{bmatrix} a_6 & b_6 & c_6 \end{bmatrix} = {\mathbf{f}_{1Z}}^T \\
&\begin{bmatrix} a_7 & b_7 & c_7 \end{bmatrix} = \frac{{\mathbf{f}_{2Y}}^T - {\mathbf{f}_{1Y}}^T}{L_e} \\
&\begin{bmatrix} a_8 & b_8 & c_8 \end{bmatrix} = \frac{{\mathbf{f}_{2Z}}^T - {\mathbf{f}_{1Z}}^T}{L_e}
\end{aligned} \tag{2}$$

where L_e is the element length in the undeformed state. Thus, (1) can be rewritten as

$$\begin{aligned}
\mathbf{f}(\mathbf{X}) = {} & \mathbf{f}_1 + \mathbf{f}_{1X} X - \left[\frac{\mathbf{f}_{2X} + 2\mathbf{f}_{1X}}{L_e} - \frac{3(\mathbf{f}_2 - \mathbf{f}_1)}{{L_e}^2} \right] X^2 \\
& + \left[\frac{\mathbf{f}_{2X} + \mathbf{f}_{1X}}{{L_e}^2} + \frac{2(\mathbf{f}_1 - \mathbf{f}_2)}{{L_e}^3} \right] X^3 + \mathbf{f}_{1Y} Y + \mathbf{f}_{1Z} Z \\
& + \frac{\mathbf{f}_{2Y} - \mathbf{f}_{1Y}}{L_e} XY + \frac{\mathbf{f}_{2Z} - \mathbf{f}_{1Z}}{L_e} XZ.
\end{aligned} \tag{3}$$

For simplification, (3) can also be expressed by

$$\begin{aligned}
\mathbf{f}(\mathbf{X}) = \mathbf{S}(\mathbf{X}) \big[& {\mathbf{f}_1}^T \quad {\mathbf{f}_{1X}}^T \quad {\mathbf{f}_{1Y}}^T \quad {\mathbf{f}_{1Z}}^T \\
& {\mathbf{f}_2}^T \quad {\mathbf{f}_{2X}}^T \quad {\mathbf{f}_{2Y}}^T \quad {\mathbf{f}_{2Z}}^T \big]^T
\end{aligned} \tag{4}$$

where $\mathbf{S}(\mathbf{X}) = [s_1\mathbf{I} \quad s_2\mathbf{I} \quad \ldots \quad s_8\mathbf{I}]$ is a 3×24 matrix, and s_i are polynomials with respect to $\mathbf{X} = \begin{bmatrix} X & Y & Z \end{bmatrix}^T$ defined as

$$\begin{aligned} s_1 &= 1 - \frac{3X^2}{{L_e}^2} + \frac{2X^3}{{L_e}^3},\ s_2 = X - \frac{2X^2}{L_e} + \frac{2X^3}{{L_e}^2} \\ s_3 &= Y - \frac{XY}{L_e},\ s_4 = Z - \frac{XZ}{L_e}, s_5 = \frac{3X^2}{{L_e}^2} - \frac{2X^3}{{L_e}^3} \\ s_6 &= -\frac{X^2}{L_e} + \frac{X^3}{{L_e}^2}, s_7 = \frac{XY}{L_e}, s_8 = \frac{XZ}{L_e}. \end{aligned} \tag{5}$$

As shown in Fig. 2, when $\mathbf{f}(\mathbf{X})$ refers to the displacement field $\mathbf{r}(\mathbf{X})$ of an element, $\mathbf{f}_i = \mathbf{r}_i$ and $\mathbf{f}_{iL} = \mathbf{r}_{iL}$ will represent the nodal positions and their gradients, respectively. Then, according to (4), the expression of $\mathbf{r}(\mathbf{X})$ can be written as

$$\mathbf{r}(\mathbf{X}) = \mathbf{S}(\mathbf{X}) \begin{bmatrix} {\mathbf{q}_1}^T & {\mathbf{q}_2}^T \end{bmatrix}^T \tag{6}$$

where $\mathbf{q}_i \in \mathbb{R}^{12}$ denotes absolute nodal coordinates defined as

$$\mathbf{q}_i = \begin{bmatrix} {\mathbf{r}_i}^T & {\mathbf{r}_{iX}}^T & {\mathbf{r}_{iY}}^T & {\mathbf{r}_{iZ}}^T \end{bmatrix}^T. \tag{7}$$

Then, $\mathbf{q}_e = [{\mathbf{q}_1}^T \quad {\mathbf{q}_2}^T]^T \in \mathbb{R}^{24}$ is referred to as elemental absolute coordinates. Similarly, when $\mathbf{f}(\mathbf{X})$ refers to the field of external forces $\mathbf{w}(\mathbf{X}) \in \mathbb{R}^3$, $\mathbf{f}_i = \mathbf{w}_i \in \mathbb{R}^3$, and $\mathbf{f}_{iL} = \mathbf{w}_{iL} \in \mathbb{R}^3$ will represent the nodal payloads and their gradients. Then, the expression of $\mathbf{w}(\mathbf{X})$ can be written as

$$\mathbf{w}(\mathbf{X}) = \mathbf{S}(\mathbf{X}) \begin{bmatrix} {\mathbf{F}_1}^T & {\mathbf{F}_2}^T \end{bmatrix}^T \tag{8}$$

where $\mathbf{F}_i \in \mathbb{R}^{12}$ is referred to as absolute nodal payloads defined as

$$\mathbf{F}_i = \begin{bmatrix} {\mathbf{w}_i}^T & {\mathbf{w}_{iX}}^T & {\mathbf{w}_{iY}}^T & {\mathbf{w}_{iZ}}^T \end{bmatrix}^T. \tag{9}$$

Besides, we define $\mathbf{F}_e = [{\mathbf{F}_1}^T \quad {\mathbf{F}_2}^T]^T \in \mathbb{R}^{24}$ as the elemental absolute payload. In this sense, we achieve complete descriptions of kinematic configurations and continuously distributed forces for soft robots with finite parameters as expressed in (10) and (11), respectively

$$\mathbf{q} \in {}^{n_q} = \begin{bmatrix} {\mathbf{q}_1}^T \ {\mathbf{q}_2}^T \cdots {\mathbf{q}_n}^T \end{bmatrix}^T \tag{10}$$

$$\mathbf{F} \in {}^{n_q} = \begin{bmatrix} {\mathbf{F}_1}^T \ {\mathbf{F}_2}^T \cdots {\mathbf{F}_n}^T \end{bmatrix}^T. \tag{11}$$

We may mention that, the degree of the interpolating polynomials (1) is three, because we only use the function values and their first-order derivatives as parameters. It may not be necessary to introduce derivatives with higher orders, as the first-order positional derivatives ($\mathbf{r}_{iX}$, $\mathbf{r}_{iY}$, and $\mathbf{r}_{iZ}$) already include the information of the robot's orientation $\mathbf{R}_i$ and local deformation $\mathbf{U}_i$ at the ith node, which can be extracted using the right polar decomposition, i.e., $[\mathbf{r}_{iX} \quad \mathbf{r}_{iY} \quad \mathbf{r}_{iZ}\ ] = \mathbf{R}_i \cdot \mathbf{U}_i$ [50]. By combining this information with the function value itself, the used parameters can fully describe the motion states of the nodes. Therefore, by adjusting the number of nodes, we can fit the entire 3-D shape of the soft robot as well as the distributed forces acted on it with adjustable accuracy.

The discussed method can also be simplified for soft robots with slender structures (such as the planar soft manipulators and soft robotic fingers that will be introduced in the following sections), where the material coordinate reduces from $\mathbf{X} \in \mathbb{R}^3$ to $X \in \mathbb{R}$ (i.e., the axial arc coordinate). Hence, (1) can be simplified into

$$\mathbf{f}(X) = \begin{bmatrix} \sum_{i=1}^4 a_i X^{i-1} & \sum_{i=1}^4 b_i X^{i-1} & \sum_{i=1}^4 c_i X^{i-1} \end{bmatrix}^T. \tag{12}$$

Similar with the processes of (2)–(4), the coefficients of (12) can be obtained through Hermite interpolation method, and the resulted function can be expressed as

$$\mathbf{f}(X) = \mathbf{S}(X) \begin{bmatrix} {\mathbf{f}_1}^T & {\mathbf{f}_{1X}}^T & {\mathbf{f}_2}^T & {\mathbf{f}_{2X}}^T \end{bmatrix}^T \tag{13}$$

where $\mathbf{S}(X) = [s_1\mathbf{I} \quad s_2\mathbf{I} \quad s_3\mathbf{I} \quad s_4\mathbf{I}]$ with $s_i\ (i = 1, 2, 3, 4)$ defined as

$$\begin{aligned} s_1 &= \frac{2X^3}{{L_e}^3} - \frac{3X^2}{{L_e}^2} + 1, s_2 = \frac{X^3}{{L_e}^2} - \frac{2X^2}{L_e} + X \\ s_3 &= -\frac{2X^3}{{L_e}^3} + \frac{3X^2}{{L_e}^2}, s_4 = \frac{X^3}{{L_e}^2} - \frac{X^2}{L_e}. \end{aligned} \tag{14}$$

In addition, the expressions of absolute nodal coordinates and absolute nodal payloads are reduced from (7) and (9) to (15)

$$\mathbf{q}_i = \begin{bmatrix} {\mathbf{r}_i}^T & {\mathbf{r}_{iX}}^T \end{bmatrix}^T, \mathbf{F}_i = \begin{bmatrix} {\mathbf{w}_i}^T & {\mathbf{w}_{iX}}^T \end{bmatrix}^T. \tag{15}$$

Thus, the resulted elemental displacement field and the external force field can be rewritten as

$$\begin{aligned} \mathbf{r}(X) &= \mathbf{S}(X) \begin{bmatrix} {\mathbf{q}_1}^T & {\mathbf{q}_2}^T \end{bmatrix}^T \\ \mathbf{w}(X) &= \mathbf{S}(X) \begin{bmatrix} {\mathbf{F}_1}^T & {\mathbf{F}_2}^T \end{bmatrix}^T. \end{aligned} \tag{16}$$

For soft robots under low-speed conditions, the equilibrium equation below should be satisfied

$$\mathbf{Q}(\mathbf{F}, \mathbf{q}, \mathbf{P}) = \mathbf{Q}_F(\mathbf{F}) + \mathbf{Q}_E(\mathbf{q}) + \mathbf{Q}_A(\mathbf{q}, \mathbf{P}) = \mathbf{0} \tag{17}$$

where $\mathbf{Q}_F$, $\mathbf{Q}_E$, and $\mathbf{Q}_A \in \mathbb{R}^{n_q}$ are the generalized force vectors corresponding to external payloads (including the gravity), elasticity, and actuation, respectively, and $\mathbf{Q}$ represents the total generalized force of the system. The expression of $\mathbf{Q}_A$ and $\mathbf{Q}_E$ can be obtained according to the following:

$$\mathbf{Q}_A(\mathbf{q}, \mathbf{P}) = \frac{\partial W_A(\mathbf{q}, \mathbf{P})}{\partial \mathbf{q}} \tag{18}$$

$$\mathbf{Q}_E(\mathbf{q}) = -\frac{U_E(\mathbf{q})}{\partial \mathbf{q}} \tag{19}$$

where W_A is the work done by the actuation forces and U_E represents the elastic potential energy of the soft structure. With linear elastic assumptions, the derivation of W_A and U_E for spatial and planar pneumatic soft robots have been reported in [48] and [49], respectively. Besides, the expression of $\mathbf{Q}_F$ can be obtained with the virtual work principle. For one element of the soft robot, the virtual work done by the payload $\mathbf{w}(\mathbf{X})$ can be calculated as

$$\delta W_F(\mathbf{F}) = \int_V \delta\mathbf{r}(\mathbf{X})^T \mathbf{w}(\mathbf{X})\, d\mathbf{X}. \tag{20}$$

Substituting (6) and (8) (or (16)) into (20), the result is given as

$$\delta W_F(\mathbf{F}) = \delta{\mathbf{q}_e}^T \left[\int_V \mathbf{S}(\mathbf{X})^T \mathbf{S}(\mathbf{X})\, d\mathbf{X}\right] \mathbf{F}_e. \tag{21}$$

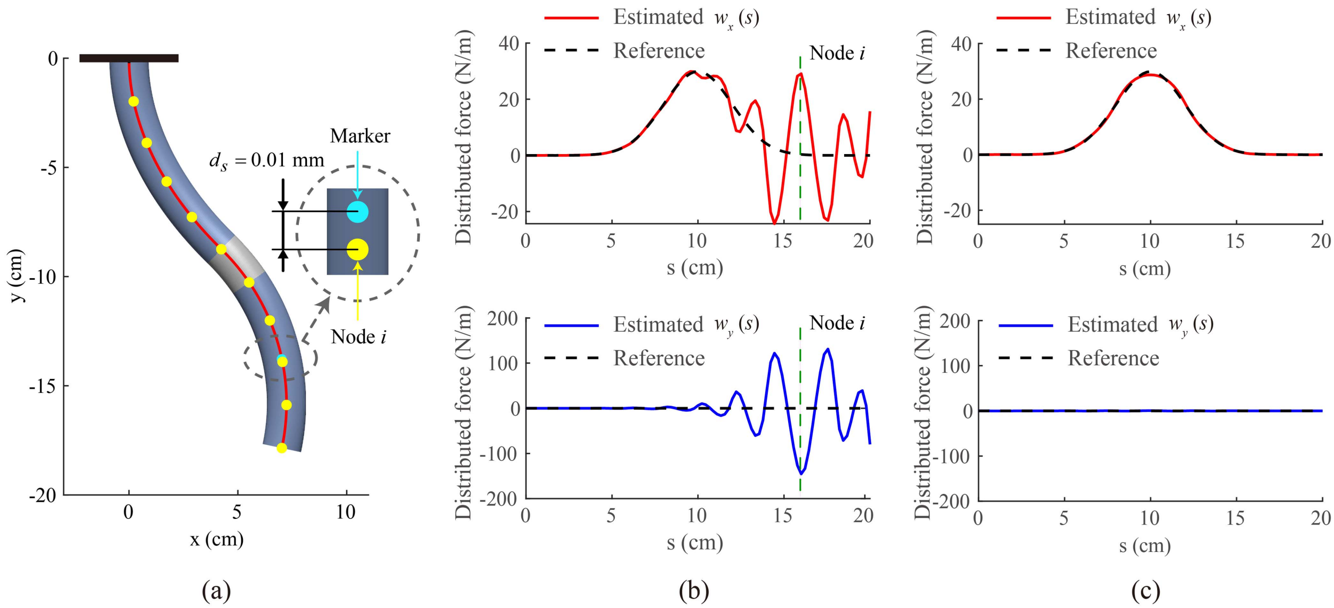

Fig. 3. Comparisons between our developed estimator and the direct solution based on (24) when the robot configuration is completely measured. (a) Schematic illustration of the small error ($d_s = 0.01$ mm) existing in the measurement of the ith node's position. (b) Estimated forces distributed on the robot by (24) are compared with the reference. (c) Effects of our developed estimation method.

Hence, the elemental generalized force $\mathbf{Q}_F^e$ is obtained as

$$\mathbf{Q}_F^e(\mathbf{F}_e) = \left[\int_V \mathbf{S}(\mathbf{X})^T \mathbf{S}(\mathbf{X})\, d\mathbf{X}\right] \mathbf{F}_e. \tag{22}$$

Assembling the result of (22) of all the elements, the global generalized force vector $\mathbf{Q}_F$ can be obtained. According to (22), it is notable that $\mathbf{Q}_F$ is linear with the defined payload parameters $\mathbf{F}$. Therefore, we can also express $\mathbf{Q}_F$ in the following form:

$$\mathbf{Q}_F = \mathbf{J}_{QF}\mathbf{F} \tag{23}$$

where $\mathbf{J}_{QF} \in \mathbb{R}^{n_q \times n_q}$ is a constant matrix for a soft robot.

The linear relationship (23) is brought by our parametric construction of the continuous payload function $\mathbf{w}(\mathbf{X})$. This feature can further contribute to an analytical Jacobian-based mapping between the robot configuration $\mathbf{q}$ and $\mathbf{F}$, which is crucial for the design of the multimodal estimator in this work. We will demonstrate this point in the following Section III.

III. Motion-Force Multimodal Estimation

When the actuation pressures $\mathbf{P}$ is given, the parametric model (17) describes the relationship between the configuration variables $\mathbf{q}$ and the parameters of distributed forces $\mathbf{F}$, making it possible for us to estimate the external forces by the measured robot configuration. However, it is not easy to obtain a complete measurement of the soft robot's configuration, especially for the positional derivatives that include the information of orientation and material deformation at all the defined nodes. In addition, errors in motion measurement can lead to serious errors in force estimation. To address these issues, this section aims to develop an algorithm to estimate both the complete kinematic configuration $\mathbf{q}$ and parameters of external payloads $\mathbf{F}$ purely by limited motion measurement information. According to the multiple outputs ($\mathbf{q}$ and $\mathbf{F}$) of this algorithm, we refer to it as a motion-force multimodal estimator in this article.

Before introducing this multimodal estimation method, we first introduce the calculation of the payload parameter $\mathbf{F}$ when the robot's configuration variable $\mathbf{q}$ can be fully measured. We may mention that, with the given values of the kinematic configuration $\mathbf{q}$ and the actuation pressures $\mathbf{P}$, the generalized force vectors $\mathbf{Q}_E$, and $\mathbf{Q}_A$ can be both calculated out by (18) and (19), respectively. Then, $\mathbf{Q}_F$ can be also obtained with (17). Therefore, if the robot configuration $\mathbf{q}$ is fully measured, the parameters of distributed external forces acted on the robot can be directly calculated out by (23), and the result reads as

$$\mathbf{F} = -(\mathbf{J}_{QF})^{-1}\left[\mathbf{Q}_E(\mathbf{q}) + \mathbf{Q}_A(\mathbf{q}, \mathbf{P})\right]. \tag{24}$$

However, the result of (24) could be extremely sensitive to the measurement errors of the robot configuration due to the anisotropic structure stiffness. We would like to clarify this point with the following simulation tests (see also in Fig. 3): We discrete a simulated two-section soft robot (with the length of 20 cm, flexural rigidity of 0.02 $\mathrm{N \cdot m^2}$, and tensile rigidity of 300 N) into 10 elements. The positions and orientations of the robot are completely measured in all the defined nodes. However, a very small error ($d_s = 0.01$ mm) exists for the measurement of the ith node's position [as shown in Fig. 3(a)]. Even the measurement error is such a small one, large errors will be produced in the calculation of external forces [as shown in Fig. 3(b)]. The reason is that, with distributed forces, the robot will easily bend due to its slender structure, but it can difficultly elongate due to the large elongation stiffness. Therefore, small measurement error of the robot configuration will produce large estimated force in the axial direction (the large-stiffness direction).

Besides the sensitivity to the measurement error, (24) requires the data of the complete robot configuration, which could be difficult in practice. In common cases, we can only obtain a part of configuration information $\mathbf{Aq} \in \mathbb{R}^{n_{ob}}$, where $\mathbf{A} \in \mathbb{R}^{n_{ob} \times n_q}$ is a constant selection matrix. To address the issues, we can formulate the following optimization model to estimate both the actual kinematic configuration $\mathbf{q}$ and parameters of distributed forces $\mathbf{F}$ with the observed value of $\mathbf{Aq}$ (denoted as $\bar{\mathbf{q}}_{ob}$):

$$\min_{\mathbf{q},\mathbf{F}} \left(\mathbf{Aq} - \bar{\mathbf{q}}_{ob}\right)^T \mathbf{W} \left(\mathbf{Aq} - \bar{\mathbf{q}}_{ob}\right) + H\left(\mathbf{F}\right)$$
$$\text{subject to } \mathbf{Q}\left(\mathbf{F}, \mathbf{q}, \mathbf{P}\right) = \mathbf{0} \tag{25}$$

where $\mathbf{W}$ is a constant diagonal matrix of weight coefficients and $H(\cdot)$ is a penalty function defined as

$$H\left(\mathbf{F}\right) = \alpha \sum_{i=1}^{n_e} \int_0^{L_i} \mathbf{w}_i(X)^T \mathbf{w}_i(X) dX \tag{26}$$

with n_e, L_i, $\mathbf{w}_i(X)$, and α denoting the number of discrete elements, elemental length, the payload function of the ith element, and a constant coefficient, respectively. Substituting (16) into (26), the expression of $H(\mathbf{F})$ can be simplified into $H(\mathbf{F}) = \alpha \mathbf{F}^T \mathbf{B} \mathbf{F}$, where $\mathbf{B} \in \mathbb{R}^{n_q \times n_q}$ is a constant matrix. In this optimization model, we do not impose $\mathbf{Aq} = \bar{\mathbf{q}}_{ob}$ to the estimated result of $\mathbf{q}$. Instead, we allow the existence of small deviation between the estimated robot configuration and the measured data. This is achieved by the designed objective function in (25). There are two terms in this function. The first term makes $\mathbf{Aq}$ close to $\bar{\mathbf{q}}_{ob}$, while the penalty function prevents the severe estimation error of forces caused by the anisotropic stiffness and measurement errors.

Nevertheless, it is difficult to solve the optimization model (25) directly due to the nonlinear constraint equations. We may mention that the constraint equation used in (25) actually represent the relation among $\mathbf{F}$, $\mathbf{q}$, and $\mathbf{P}$. Thus, we can regard the configuration parameters $\mathbf{q}$ as a function of the payload parameters $\mathbf{F}$ (with the value of $\mathbf{P}$ given), and rewrite (25) into the following unconstrained optimization model:

$$\min_{\mathbf{F}} g\left(\mathbf{F}\right) = \left(\mathbf{Aq}\left(\mathbf{F}\right) - \bar{\mathbf{q}}_{ob}\right)^T \mathbf{W} \left(\mathbf{Aq}\left(\mathbf{F}\right) - \bar{\mathbf{q}}_{ob}\right) + H\left(\mathbf{F}\right). \tag{27}$$

Although the computation of $\mathbf{q}(\mathbf{F})$ relies on numerical algorithm, by combining (17) and (23), we can analytically calculate the gradient of $\mathbf{q}(\mathbf{F})$ as

$$\mathbf{J}_{qF} \in \mathbb{R}^{n_q \times n_q} = \frac{\partial \mathbf{q}}{\partial \mathbf{F}} = -\left[\frac{\partial\left(\mathbf{Q}_A + \mathbf{Q}_E\right)}{\partial \mathbf{q}}\right]^{-1} \mathbf{J}_{QF}. \tag{28}$$

Thanks to this analytical Jacobian-based mapping between $\mathbf{q}$ and payload parameters $\mathbf{F}$, the gradient of the objective function $g(\mathbf{F})$ can be expressed analytically as

$$\frac{\partial g\left(\mathbf{F}\right)}{\partial \mathbf{F}} = \left[2\left(\mathbf{q}(\mathbf{F})^T \mathbf{A}^T - \bar{\mathbf{q}}_{ob}^T\right) \mathbf{WAJ}_{qF}\right]^T + 2\alpha \mathbf{BF} = \mathbf{0}. \tag{29}$$

The Hessian matrix of $g(\mathbf{F})$ is subsequently obtained as

$$\frac{\partial^2 g\left(\mathbf{F}\right)}{\partial \mathbf{F}^2} = 2{\mathbf{J}_{qF}}^T \mathbf{A}^T \mathbf{WAJ}_{qF} + 2\alpha \mathbf{B}. \tag{30}$$

In the formulas above, we utilize the differentiable relation between the robot configurations $\mathbf{q}$ and payload parameters $\mathbf{F}$, which contributes to the analytical expressions in (29) and (30). Hence, we can efficiently solve the obtained unconstrained optimization model (27) using classical Newton's method. This algorithm can achieve convergence to the optimal solution $\mathbf{F}^*$ when the Hessian matrix is positive definite and the initial value of the vector $\mathbf{F}$ is near the solution [51]. Therefore, we set the values of $\mathbf{W}$ and α to ensure the positive definiteness of (30). In addition, for the ith control step, we use the solution of the last step $\mathbf{F}_{i-1}^*$ as the initial value. Meanwhile, to avoid the influence of the rapidly changing forces between two steps on the convergence, we generate an incremental sequence of the input sensor information from $\bar{\mathbf{q}}_{ob}^{i-1}$ to $\bar{\mathbf{q}}_{ob}^{i}$ and solve the optimization model successively according to the sequence. By these ways, the convergence of the algorithm can thus be ensured.

As shown in Fig. 3(c), by using this method, the estimated errors caused by the measurement inaccuracy are almost eliminated. Besides the result shown in Fig. 3(c) where $\mathbf{q}$ is completely measured for force estimation, our developed method can also use limited data to estimate the complete robot configurations and distributed forces. This point can be demonstrated by the following simulation test. We divide the aforementioned soft robot into 20 elements. Only parts of the nodes are served as the feature points for configuration measurement. Besides, we only use the nodal position (without the orientation information) for the motion-force estimation. As three cases, Fig. 4(a) compares the estimated forces (by different number of feature points) with the references. The average errors of the estimated backbone positions and payloads are also presented in Fig. 4(b), which are plotted as functions of the number of feature points.

The result presented above relies on the assumption that the developed physical model is completely accurate. However, in practice, the mechanical behavior of soft robots cannot exactly match the physical model due to the uncertainties like fabrication errors. With an inaccurate model, a virtual payload will be calculated out by the developed estimator even there are no actual payloads. As an illustration, Fig. 5(a) shows the estimated virtual payload induced by the errors of the actuation torque $\mathbf{M}$ and the flexural rigidity K_b, respectively. We may mention that, the effects of the calculated virtual forces to the robot motions are equivalent to the errors of the modeled mechanical behavior. Therefore, the kinematic configuration of the robot can still be well estimated even with the significant modeling errors [see Fig. 5(b) and 5(c)]. In addition, the real payload acted on the soft robot can be calculated out by subtracting the virtual payload (obtained by using the real robot moving along given trajectories without external payloads) from the estimated one. These features of the virtual payload are also verified and utilized by the applications presented in the following sections. In addition, we may note that the main feature of the developed estimation algorithm is that it can obtain the complete robot configuration as well as the external forces by limited (or inaccurate) measurement of $\mathbf{q}$. According to the definition of $\mathbf{q}$ in this work, the input of this algorithm could be partial nodal positions, orientations, or material deformations. For the convenience of experimental verifications introduced in the following sections,

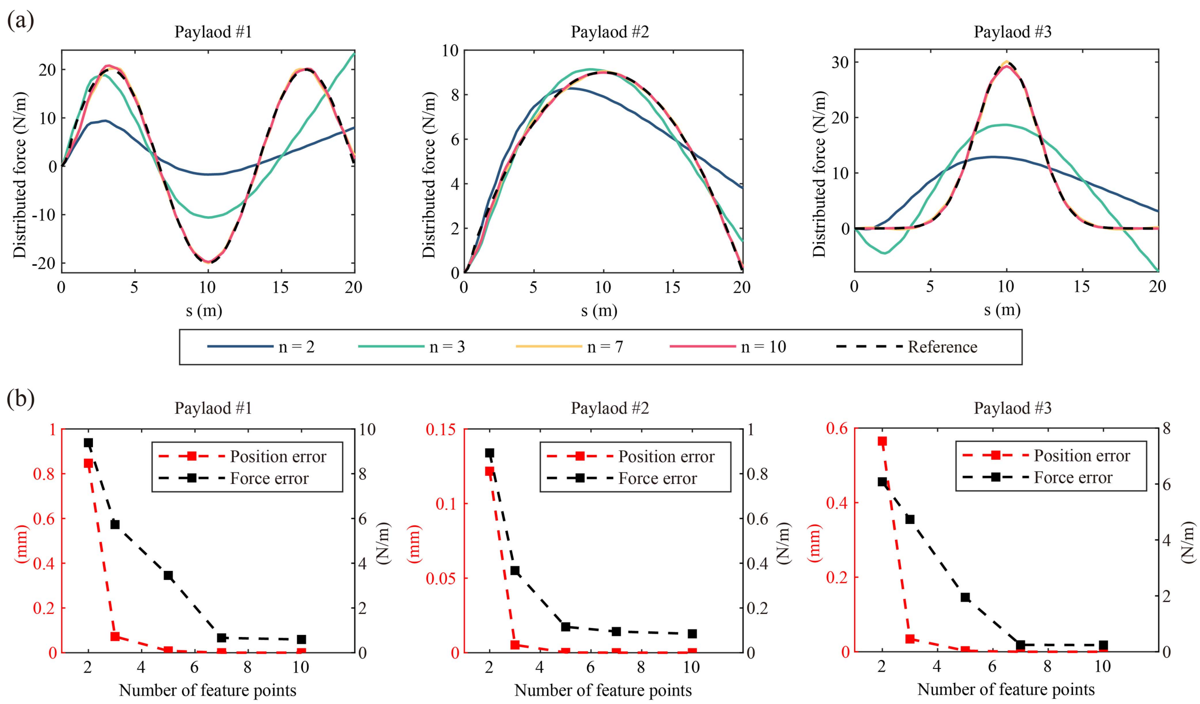

Fig. 4. Numerical validation of the developed multimodal estimator. (a) In the cases where only the positions of the feature points are measured, the estimated forces with different number of feature points are compared. (b) Estimation errors are plotted as functions of the number of feature points.

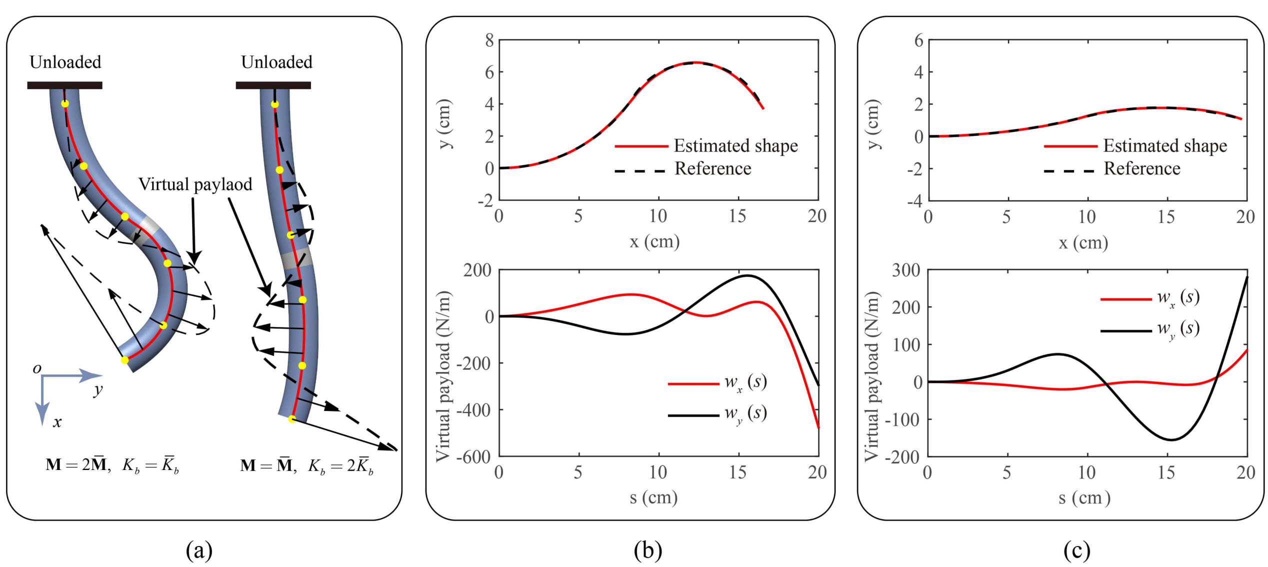

Fig. 5. Simulation illustrations of the virtual payload. (a) Effects of model errors are considered by the introduction of virtual payloads. (b)–(c) The estimated backbone shapes of the robot with inaccurate models are illustrated, along with the corresponding virtual payloads.

we will use a camera system to measure the partial information of nodal positions in this work.

IV. Precise Trajectory Tracking Control With Uncertain Forces

Utilizing the proposed multimodal estimator, we develop a control strategy specifically for soft robots operating under randomly distributed payloads. To validate the effectiveness of this controller, experiments are conducted on a two-section pneumatic soft robot [see Fig. 6(a)] with five motion capture markers attached on its backbone.

For the experimental setup, each robot section is made of two commercial PVC tubes with diameters of 18 mm (Yingli Plastic Company, Ltd.), steel wires with diameters of 0.6 mm (Xiangpeng Metal Technology Company, Ltd.), and 3-D printed

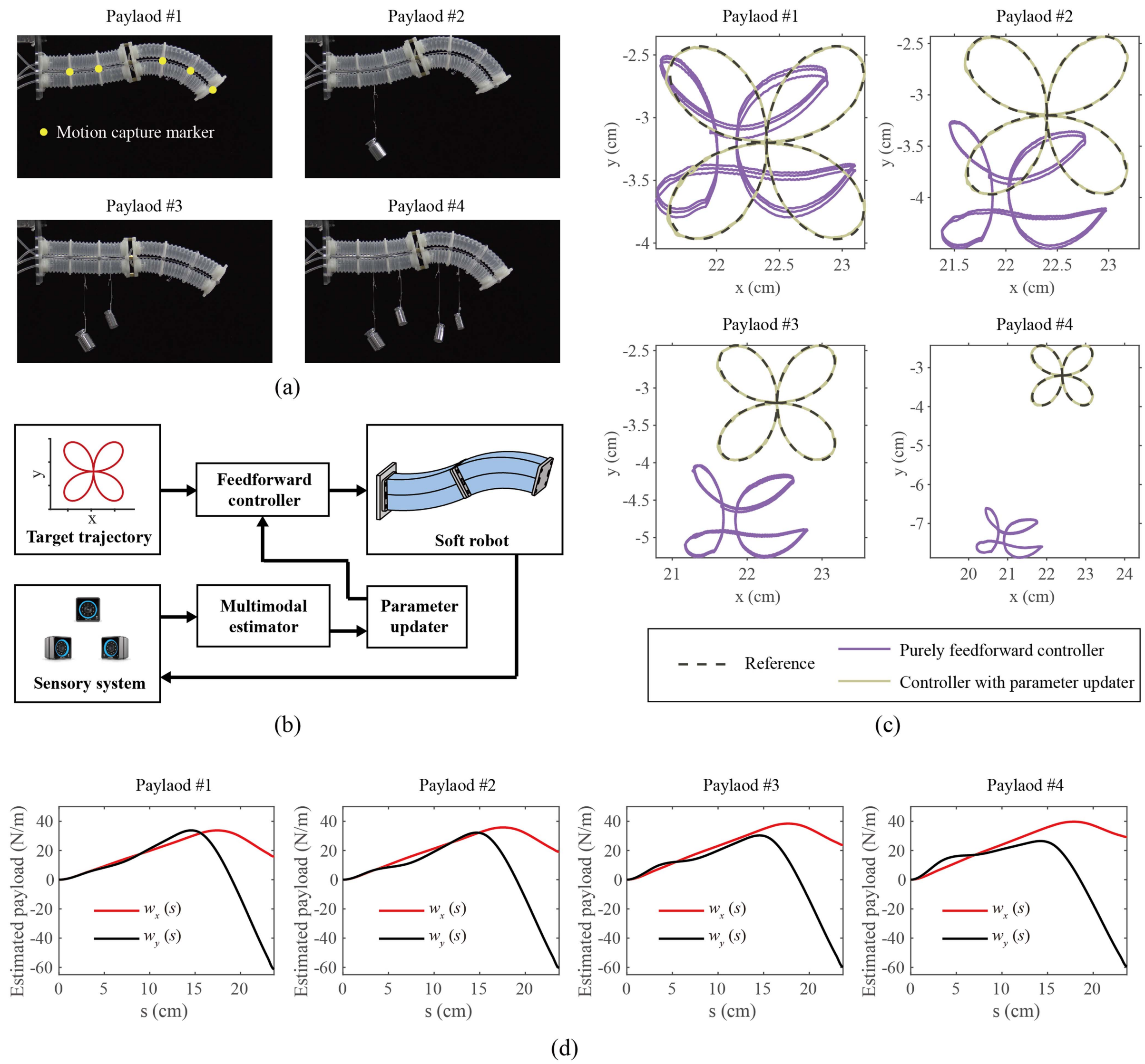

Fig. 6. Experimental results of trajectory tracking tests for the soft robot subjected to randomly distributed payloads. (a) Pictures of the used two-section soft robot subjected to arbitrary payloads. (b) Simplified illustration on the developed control strategy employed for the trajectory tracking control. (c) Comparative results of trajectory tracking tests using the developed controller with real-time parameter updater and the purely feedforward controller. (d) During the trajectory tracking tests, the average estimated forces, which include the contributions from both the external payloads and the virtual payloads, are displayed.

terminal connectors (Imagine 8000, SOMOS Inc.). The length of each robot section is 120 mm, and the flexural rigidity is 0.025 $\mathrm{N \cdot m^2}$ (identified by static loading tests [49]). To actuate the soft robot, a pneumatic regulation platform is also established. In this platform, the upper control commands of desired input pressures are sent by MATLAB run on a PC. Then, the control commands transfer to a control module (MicroLabBox-DS1202, dSPACE) by the serial port. The dc voltage signals generated by the control module are used to adjust the output pressures of electronic pressure regulators (QB1XANEEN100P400KPG, Proportion-Air). Besides, a camera system (Optitrack, Prime 13) is configured to capture the positions of markers arranged on the soft robots.

The control strategy, as shown in Fig. 6(b), comprises a feedforward controller, which utilizes the physical model to determine the actuation pressure required by the soft robot to achieve the desired trajectory. Moreover, the proposed multimodal estimator plays a crucial role in updating the controller's parameters related to the payload. In practice, the feedforward controller is implemented based on (17). In this equation, the kinematic configuration vector $\mathbf{q}$ contains the elements of the end-effector position $\mathbf{x}$. Then, given the desired end-effector position $\mathbf{x}_d$ and payload parameters $\hat{\mathbf{F}}$, the actuation pressure $\mathbf{P}$ can be obtained by solving (17) with Newton–Raphson method. Thus, we gain an inverse kinematic function $f_{IK}(\mathbf{x}_d, \hat{\mathbf{F}})$ to achieve feedforward control. Although the value of $\hat{\mathbf{F}}$ could be directly given by the result of $\bar{\mathbf{F}}$ calculated by the proposed estimation algorithm in real time, we utilize the following parameter updater to achieve better stability:

$$\dot{\hat{\mathbf{F}}} = K_P\left(\bar{\mathbf{F}} - \hat{\mathbf{F}}\right) + K_I \int \left(\bar{\mathbf{F}} - \hat{\mathbf{F}}\right) dt \tag{31}$$

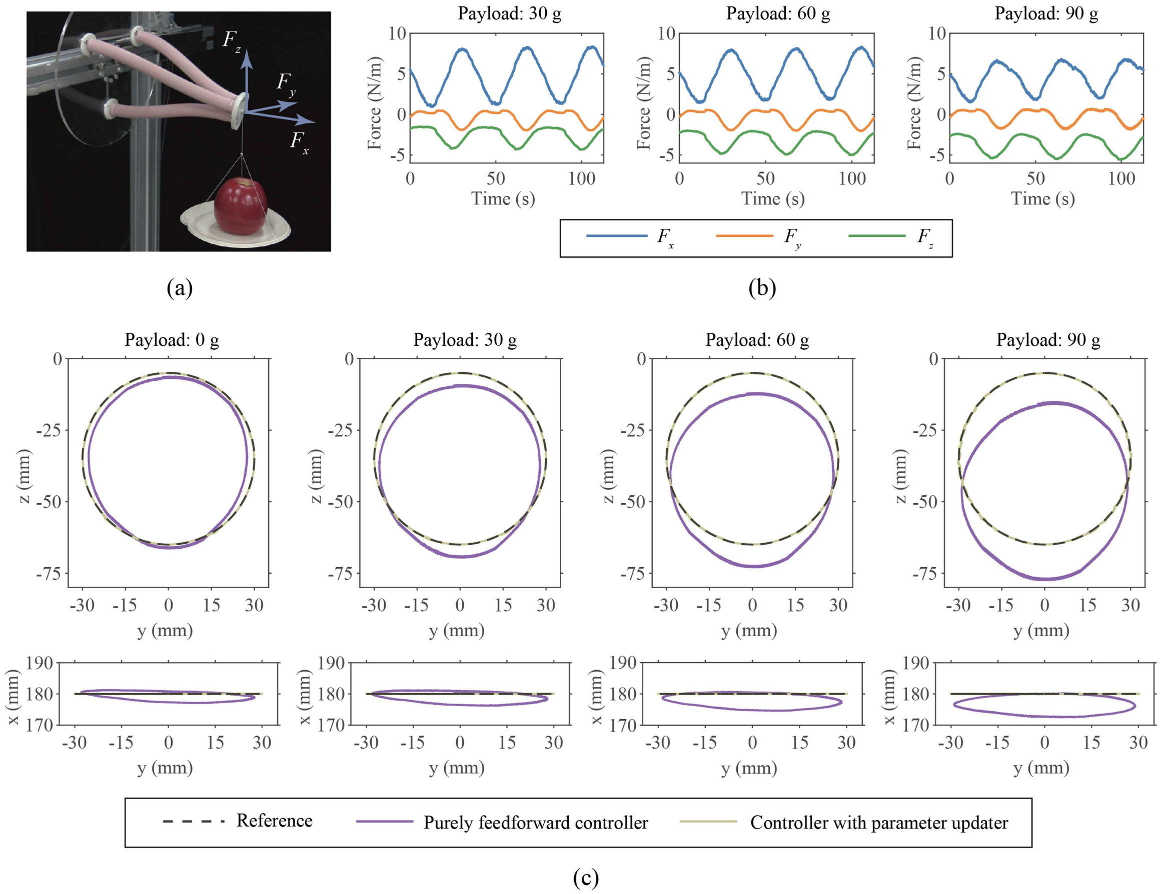

Fig. 7. Experimental results of the trajectory tracking tests with a soft parallel robot that experiences an uncertain concentrated force on its end-effector. (a) Picture of a soft parallel robot subjected to an end-effector payload. (b) Evolution of the estimated forces, including the virtual payloads, throughout the trajectory tracking tests. (c) Comparisons between the trajectory tracking results obtained with the developed controller with parameter updater and the purely feedforward controller.

Taking the derivative of (31) with respect to time, we obtain $\ddot{\hat{\mathbf{F}}} + K_P(\dot{\hat{\mathbf{F}}} - \dot{\bar{\mathbf{F}}}) + K_I(\hat{\mathbf{F}} - \bar{\mathbf{F}}) = \mathbf{0}$. Assuming that the external payloads change slowly ($\ddot{\bar{\mathbf{F}}} \approx \mathbf{0}$), the former equation can be further rewritten into $\ddot{\mathbf{e}}_F + K_P\dot{\mathbf{e}}_F + K_I\mathbf{e}_F = \mathbf{0}$, where $\mathbf{e}_F = \hat{\mathbf{F}} - \bar{\mathbf{F}}$. In this work, we set $K_P = 2\sqrt{K_I} = 4$ to ensure the parameter vector $\hat{\mathbf{F}}$ can converge to $\bar{\mathbf{F}}$ without overshoot. In addition, the resulted 2% settling time is about 1.96 s, which is sufficient for the conditions where the external forces do not change rapidly. It should be noted that the virtual payload introduced in Section III is also incorporated in $\hat{\mathbf{F}}$, enabling the parameter updater shown in Fig. 6(b) to handle the influence of modeling errors.

As presented in Fig. 6(c), we compare the performance of the purely feedforward controller (without the parameter updater) and the proposed control strategy by trajectory tracking tests with randomly distributed payloads, where the control frequency f_c is 30 Hz. The obtained average tracking error with the purely feedforward controller range from 3.2 to 43.6 mm under different payload conditions. In contrast, the developed controller with adaptive parameter updater reduced the average tracking error to a significantly lower range of 0.2 to 0.3 mm. These comparative results clearly demonstrate the effectiveness of our developed control strategy in achieving precise control with robustness against uncertain payloads.

It is worth noting that even in the payload-free case (i.e., payload #1 in Fig. 6), the purely feedforward controller still exhibited significant tracking errors. This can be attributed to the inaccuracies inherent in the physical model used by the controller. In contrast, our developed control strategy effectively compensates for this uncertainty by incorporating the virtual payload induced by modeling errors. Consequently, the controller showcases improved tracking performance across all payload conditions. In addition, the average time required for motion-force estimation and controller computation in each step is 3.2 ms. This indicates that the proposed control strategy can achieve real-time adjustment according to external disturbances (see the supplemental video Movie S1).

The proposed method can be extended to cases where it is inconvenient to configure multiple sensory units on the soft robots. For instance, in the case of a soft parallel robot comprising three soft actuators [see Fig. 7(a)], it may be challenging to directly capture the backbone motions using markers placed on the actuator surfaces. Instead, an alternative approach is to capture the position of the end-effector, which is subjected to a

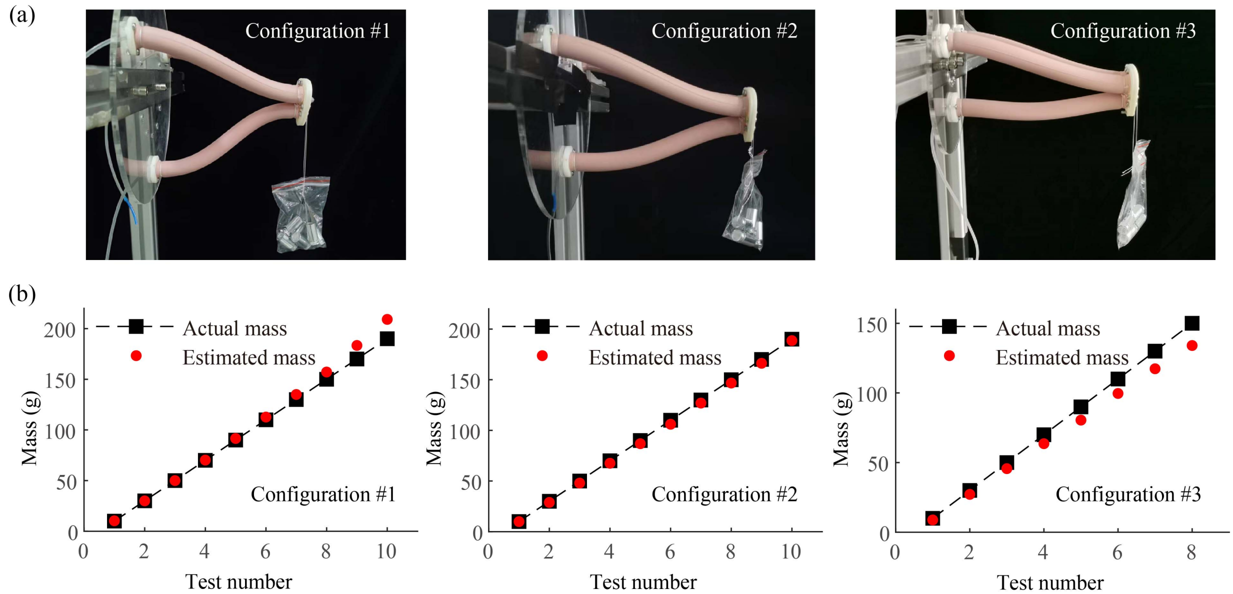

Fig. 8. Experimental results of payload estimation. (a) Pictures of soft parallel robots loaded with given weights. (b) Comparisons between the estimated mass of the hanging weights and the actual values.

concentrated payload. In such cases, our proposed method can be simplified to estimate the concentrated payload acting on a specific location. First, we can define a node at the stressed point during the discretization processes discussed in Section II. Consequently, the geometrical constraint for $\mathbf{q}$ can be written as

$$\bar{\mathbf{x}} = \mathbf{A}_x \mathbf{q} \tag{32}$$

where $\mathbf{A}_x \in \mathbb{R}^{3\times n_q}$ is a constant matrix that maps the global configuration variables $\mathbf{q}$ to the nodal position $\bar{\mathbf{x}}$. In addition, the payload parameters $\mathbf{F}$ of the soft robot can be reduced to the given nodal payload, i.e., $\mathbf{F} \in \mathbb{R}^3$. Then, the virtual work done by the concentrated payload can be calculated as

$$\mathbf{Q}_F(\mathbf{F})^T \delta\mathbf{q} = \mathbf{F}^T \delta\left(\mathbf{A}_x \mathbf{q}\right). \tag{33}$$

Hence, we obtain the generalized force of $\mathbf{F}$ with respect to the defined generalized coordinates $\mathbf{q}$, which can be expressed by

$$\mathbf{Q}_F\left(\mathbf{F}\right) = \mathbf{A}_x{}^T \mathbf{F}. \tag{34}$$

Therefore, the constraints for static equilibrium (17) can be rewritten as

$$\mathbf{Q}_E\left(\mathbf{q}\right) + \mathbf{Q}_A\left(\mathbf{q}, \mathbf{P}\right) + \mathbf{A}_x{}^T \mathbf{F} = \mathbf{0}. \tag{35}$$

By combining (32) and (35) with Newton–Raphson method, $\mathbf{q}$ and $\mathbf{F}$ can be obtained according to the given actuation pressure $\mathbf{P}$ and measured position $\bar{\mathbf{x}}$.

Using the same control architecture illustrated in Fig. 6(b), we employ the soft parallel robot to track the desired trajectory. Details of this robot are provided in [48]. Fig. 7(b) illustrates the evolution of the estimated concentrated payload, including the virtual payload, throughout the entire trajectory tracking process. The trajectories obtained using the purely feedforward controller and the controller with real-time parameter estimation are presented in Fig. 7(c). The comparative results demonstrate the robustness and precision of the proposed estimation algorithm and control strategy, with the average tracking error of 0.2 mm. Besides, we demonstrate the response of the controller to time-varying disturbances in the supplemental video Movie S2. These findings highlight the effectiveness and versatility of the developed control framework, even in scenarios where direct measurement of the backbone motions is impractical.

In addition to the high-precise trajectory tracking performance, our method can also be used to estimate the actual payloads on the soft robot. To clarify this point, we put varying weights (with the mass ranging from 0–200 g) on the soft parallel robots with three different configurations, as shown in Fig. 8(a). Then, the displacement of the end-effector is used to estimate the mass of weights. We may note that, in order to reduce the influence of the virtual payload, we use the relative displacements of the end-effector during loading rather than using the absolute position information. The experimental results are presented in Fig. 8(b), where the actual mass and the estimated one are compared. The results show that the average estimation errors under the three configurations are 4.9 g, 2.4 g, and 7.9 g, respectively.

V. Automatic Obstacle Avoidance

In certain application scenarios, such as exploration and rescue missions, robots are often required to operate in unstructured environments with uncertain obstacles. Soft robots offer great potential for such scenarios, as they are compliant and can provide safe interaction with the environment. However, it is elusive to endow soft robots with the adaptability under uncertain contacts. In this study, we demonstrate that our developed multimodal estimator and control framework can be used for obstacle perception and automatic motion control when uncertain contact occurs.

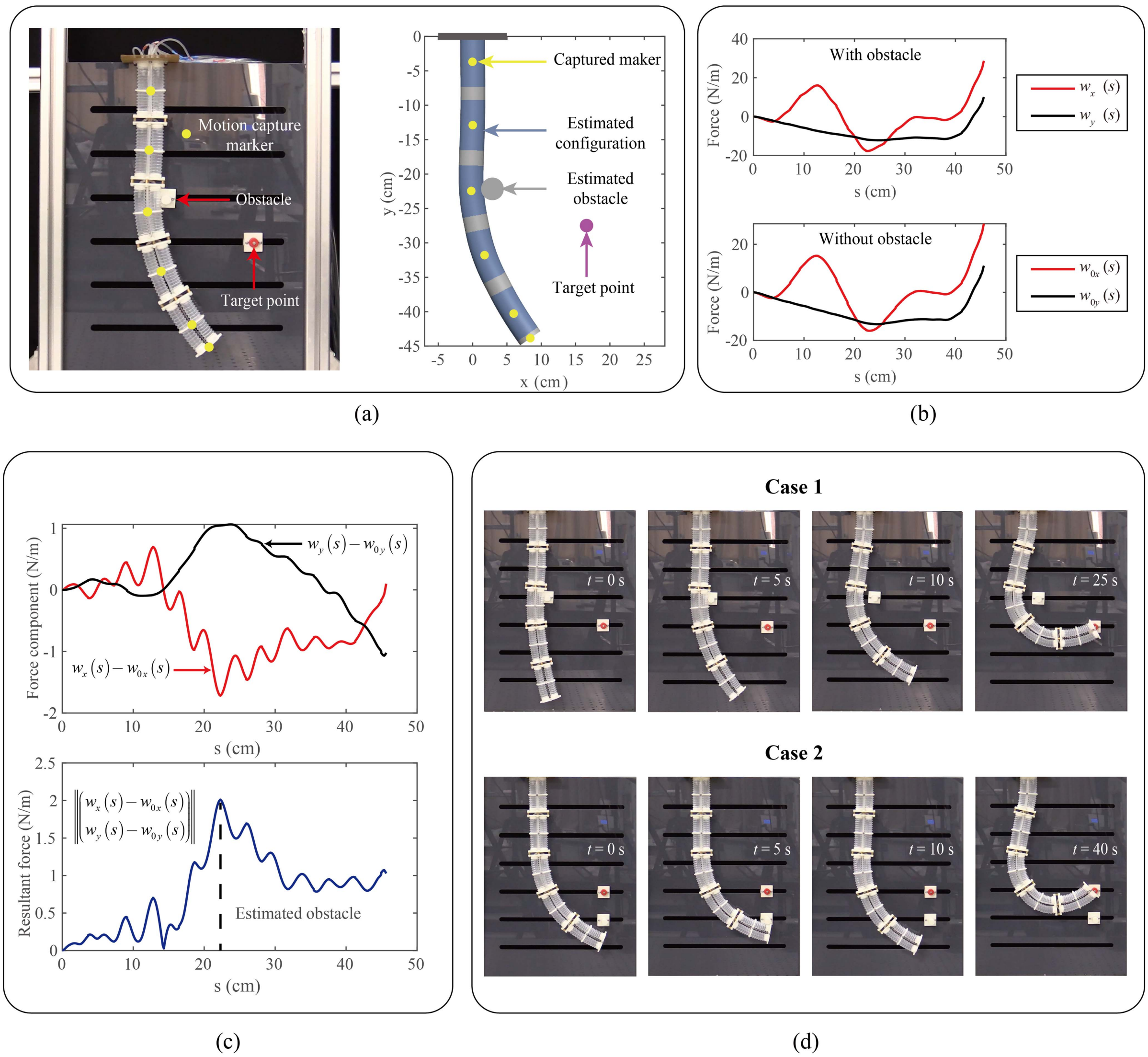

Fig. 9. Experimental results of autonomous obstacle avoidance for soft robots. (a) Comparisons between the real state and estimated configuration of a five-section soft robot when contacting with an obstacle. (b) Comparisons of estimated forces, including the virtual forces, in the presence and absence of an obstacle. (c) Estimation result of the real force distribution is obtained by subtracting the virtual payload from the estimated one. (d) Pictures showing the sequential processes of the soft robot: contacting the obstacle, recognizing its presence, avoiding it, and eventually reaching the target point.

To this end, we fabricate a five-section pneumatic soft robot operating within a confined environment, as shown in Fig. 9(a). The length of each robot section is 93 mm, while other details of this robot are the same to the two-section robot introduced in Section IV. Our proposed motion-force multimodal estimation strategy is implemented on this robot, allowing us to estimate the external forces acting on the robot (with six motion capture markers) and thereby determine the position of contacting obstacles. To minimize the influence of model inaccuracies on obstacle perception, we initially guide the robot along a predetermined trajectory without obstacles and record the estimated virtual payload. As shown in Fig. 9(b), when the contact first occurs, the contact force is small, resulting in the estimated force being close to the previously recorded virtual payload without the obstacle. However, by directly subtracting, we can extract the real distribution of the contact force, as shown in Fig. 9(c). The peak of this obtained force distribution indicates the obstacle's location, with an estimated error of approximately 1.5 cm compared to the actual obstacle position. It should be noted that the accuracy of this estimation is dependent on the density of the measured feature points. In our experimental setup, we use six motion capture markers arranged on the rigid connectors and the end-effector of the robot, which is proved sufficient for the obstacle avoidance tasks discussed in this section.

To enable automatic target reaching with obstacle avoidance, we develop a shape kinematic control strategy for the multisectional soft robots. This feedback strategy combines the artificial potential field algorithm [52] with our established model, which is discussed in the following. The approach involves constructing two artificial potential fields: an attractive field and a repulsive field. The attractive field is utilized to adjust the position of the end-effector toward the desired target point. The attractive potential function can be expressed by

$$U_{\text{att}} = \zeta \left\| \mathbf{x}_e - \mathbf{x}_{\text{goal}} \right\| \tag{36}$$

where $\mathbf{x}_e$ and $\mathbf{x}_{\text{goal}}$ represent the positions of the end-effector and the target point, respectively, and ζ is a positive constant related to the field magnitude. The gradients of U_{att} with respect to $\mathbf{x}_e$ always points from the target point to the end-effector

$$\frac{\partial U_{\text{att}}}{\partial \mathbf{x}_e} = \frac{\zeta}{\left\| \mathbf{x}_e - \mathbf{x}_{\text{goal}} \right\|} \left(\mathbf{x}_e - \mathbf{x}_{\text{goal}} \right). \tag{37}$$

Furthermore, the repulsive field U_{rep} is employed to influence the selected control points of the soft robot. These control points are determined as the points closest to the obstacle for each discretized element, with a constraint that the distance to the obstacle should be within a specified parameter Q_0. Let $\mathbf{x}_{ci}$ denote the position of the ith control point and $\mathbf{x}_{\text{obs}}$ represent the position of the obstacle. The expression of U_{rep}, the repulsive potential function, can be written as

$$U_{\text{rep}} = \sum_{i=1}^{n_c} \alpha_r \left(\frac{1}{\left\| \mathbf{x}_{ci} - \mathbf{x}_{\text{obs}} \right\|} - \frac{1}{Q_0} \right)^2 \tag{38}$$

where α_r is a positive constant. The gradients of U_{rep} with respect to $\mathbf{x}_{ci}$ point from the control points to the obstacle, which can be found in

$$\frac{\partial U_{\text{rep}}}{\partial \mathbf{x}_{ci}} = \alpha \left(\frac{1}{Q_0} - \frac{1}{\left\| \mathbf{x}_{ci} - \mathbf{x}_{\text{obs}} \right\|} \right) \frac{\mathbf{x}_{ci} - \mathbf{x}_{\text{obs}}}{\left\| \mathbf{x}_{ci} - \mathbf{x}_{\text{obs}} \right\|^{3/2}}. \tag{39}$$

In quasi-static conditions, $\mathbf{x}_{ci}$ and $\mathbf{x}_e$ are controlled by the actuation pressures $\mathbf{P}$ of the robot. Hence, the resultant field $U_t = U_{\text{att}} + U_{\text{rep}}$ can be considered as a function of $\mathbf{P}$. In order to control the end-effector to the target while avoiding the obstacle, we apply the following control strategy based on gradient descent:

$$\dot{\mathbf{P}} = -\beta \frac{\partial U_t}{\partial \mathbf{P}} \tag{40}$$

denoting β as a positive coefficient determining the output velocity of the robot. According to the chain rule, $\partial U_t / \partial \mathbf{P}$ can be calculated by

$$\frac{\partial U_t}{\partial \mathbf{P}} = \frac{\partial U_t}{\partial \mathbf{X}_c} \frac{\partial \mathbf{X}_c}{\partial \mathbf{q}} \frac{\partial \mathbf{q}}{\partial \mathbf{P}} \tag{41}$$

where $\mathbf{X}_c$ is a vector assembled by the positions of control points and the end-effector, as defined in

$$\mathbf{X}_c = \left[\mathbf{x}_{c1}{}^T \quad \mathbf{x}_{c2}{}^T \quad \ldots \quad \mathbf{x}_{cn_c}{}^T \quad \mathbf{x}_e{}^T \right]^T. \tag{42}$$

In (41), $\partial U_t / \partial \mathbf{X}_c$ and $\partial \mathbf{X}_c / \partial \mathbf{q}$ can be obtained according to (36), (38), and (16). Besides, the actuation Jacobian $\partial \mathbf{q} / \partial \mathbf{P}$ can be derived by the equilibrium equation (17) with the result written as

$$\frac{\partial \mathbf{q}}{\partial \mathbf{P}} = -\left(\frac{\partial \mathbf{Q}}{\partial \mathbf{q}} \right)^{-1} \frac{\partial \mathbf{Q}}{\partial \mathbf{P}}. \tag{43}$$

Under the conditions that the actuation pressures are close to the given bounds with the strategy (40), the relevant elements of $\dot{\mathbf{P}}$ are adjusted to zeros. In addition, with the given output velocity v_d of the end-effector, the coefficient β can be set as

$$\beta = v_d / \left\| \frac{\partial \mathbf{x}_e}{\partial \mathbf{q}} \frac{\partial \mathbf{q}}{\partial \mathbf{P}} \frac{\partial U_t}{\partial \mathbf{P}} \right\|. \tag{44}$$

In experiments, the parameters of this obstacle avoidance strategy are given as: $Q_0 = 10$ cm, $\alpha_r = 0.02$, $\zeta = 200$, $v_d = 5$ mm/s, and control frequency $f_c = 20$ Hz.

By combining the obstacle perception capabilities provided by the multimodal estimator with the above control strategy, the soft robot is able to autonomously navigate toward a given target while avoiding obstacles. Two cases are presented in Fig. 9(d), illustrating the process of the robot contacting the obstacle, avoiding it, and eventually reaching the target. A demonstration video is also provided in Movie S3.

VI. Adaptive Robotic Grasp

Soft robots are particularly well-suited for robotic grasping applications, especially when handling fragile objects. However, planning and controlling the motions of soft grippers in the presence of object uncertainties can be challenging, leading to unreliable grasping outcomes. In this work, with the integration of the proposed motion-force multimodal estimator, we develop a model-based adaptive pinch grasp strategy for a kind of soft robotic grippers.

Fig. 10(a) presents the design of the used two-finger soft robotic gripper with major dimensions. Each finger of the gripper owns two soft segments composed by two actuator elements and a strain-limiting layer. Applying compressed air to the chamber of either actuator element, bending deformation of the finger segment can be produced. The fiber wound around the chamber is used to avoid the shape change of the segment's cross section. Besides, the strain-limiting layer is used to prevent the segment from elongation. The pneumatic actuation effect of such planar soft mechanisms can be modeled as pairs of concentrated actuation torques [49] acted on the two ends of each finger segment.

When the soft gripper makes contact with an object, the proposed motion-force estimator can be used to determine the contact point by the estimated distributions of contact forces, as illustrated in Fig. 10(b). Besides, we develop and implement an adaptive grasp strategy for the soft gripper that aims to adjust the contact angle between the gripper surface and the object while maximizing the output forces, thereby achieving high reliability during the grasping process.

Considering the symmetry of the designed soft robotic gripper, here, we only discuss the control strategy of the left finger to avoid redundancy. First, we need to establish the relationship between actuation pressures $\mathbf{P}$ and poses of the robotic finger at the contact point. According to (16), the shape of the element c (where the contact occurs) can be written as

$$\mathbf{r}(X) = \mathbf{S}(X) \mathbf{q}_{ec} \tag{45}$$

where $\mathbf{q}_{ec} = \mathbf{A}_e \mathbf{q}$ is a subvector of $\mathbf{q}$ with $\mathbf{A}_e$ being a constant matrix. Then, the position of the contact point $\mathbf{x}_c$ can be expressed by

$$\mathbf{p}_c = \mathbf{S}\left(X_c \right) \mathbf{q}_{ec} \tag{46}$$

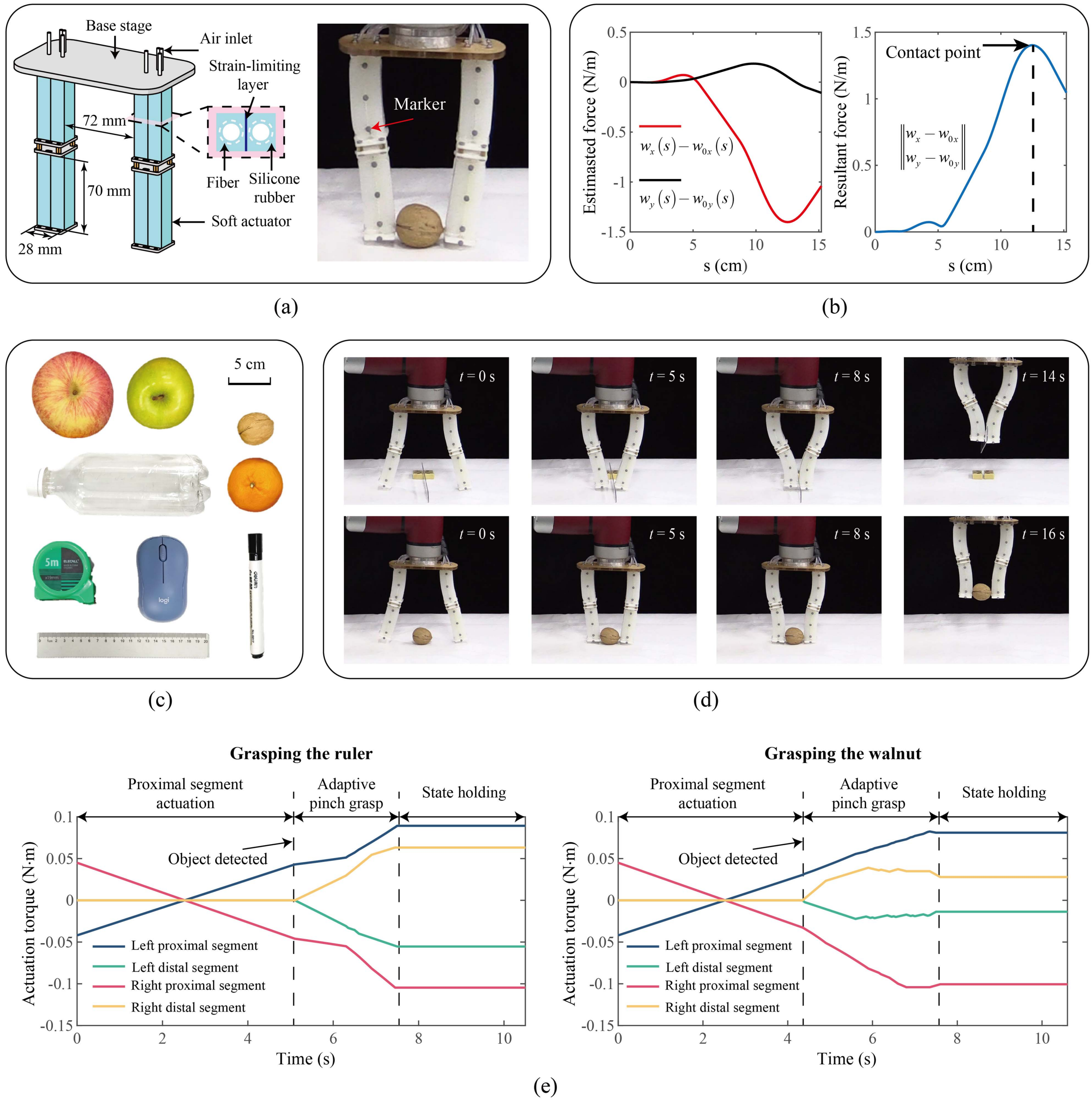

Fig. 10. Verification of the adaptive grasp strategy based on the developed model-based control framework. (a) Design illustration and a picture of the soft gripper. (b) Contact point between the soft gripper and the manipulated object is estimated according to the result of force estimation. (c) Objects with different sizes and shapes are used for the verification of our developed method. (d) Processes of adaptive grasping through two specific cases. (e) Evolutions of the applied actuation torque of the gripper in different phases: linear proximal segment actuation before the object is detected, adaptive pinch grasping, and state holding.

with X_c representing the arc coordinate of contact point in element c. Besides, the axial direction vector η of the finger at the contact point reads as

$$\eta = \frac{\partial \mathbf{r}(X)}{\partial X}|_{X=X_c} = \frac{\partial \mathbf{S}(X)}{\partial X}|_{X=X_c}\mathbf{q}_{ec}. \quad (47)$$

Denoting the vertical direction vector as $\eta_0 = [0 \quad -1 \quad 0]^T$, the angle θ between η_0 and η can be calculated as

$$\theta = \arcsin\left(\|\eta \times \eta_0\|\right). \quad (48)$$

Assembling (46) and (48), the finger pose at the contact point can be obtained as

$$\mathbf{x}_c\left(\mathbf{q}_{ec}\right) = \left[\mathbf{p}_c{}^T \quad \theta\right]^T. \quad (49)$$

According to (17) and the result of (49), the Jacobian that maps the actuation pressures to the finger pose $\mathbf{x}_c$ given as

$$\mathbf{J}_c = \frac{\partial \dot{\mathbf{x}}_c}{\partial \dot{\mathbf{P}}} = -\frac{\partial \mathbf{x}_c}{\partial \mathbf{q}_{ec}}\mathbf{A}_e\left(\frac{\partial \mathbf{Q}}{\partial \mathbf{q}}\right)^{-1}\frac{\partial \mathbf{Q}}{\partial \mathbf{P}}. \quad (50)$$

To achieve reliable pinch grasp, we should ensure the convergence of contact angle θ to zero while enlarge the contact force

TABLE I
SUCCESS RATES OF THE GRASPING TESTS WITH DIFFERENT CONTROL STRATEGIES (FIVE REPETITIONS FOR EACH OBJECT)

Object	Ruler	Marking pen	Green apple	Plastic bottle	Tangerine	Red apple	Mouse	Tape measure	Walnut
Adaptive grasp strategy	100%	100%	100%	100%	100%	100%	100%	100%	100%
Open-loop grasp strategy	40%	0%	60%	20%	100%	0%	100%	0%	20%

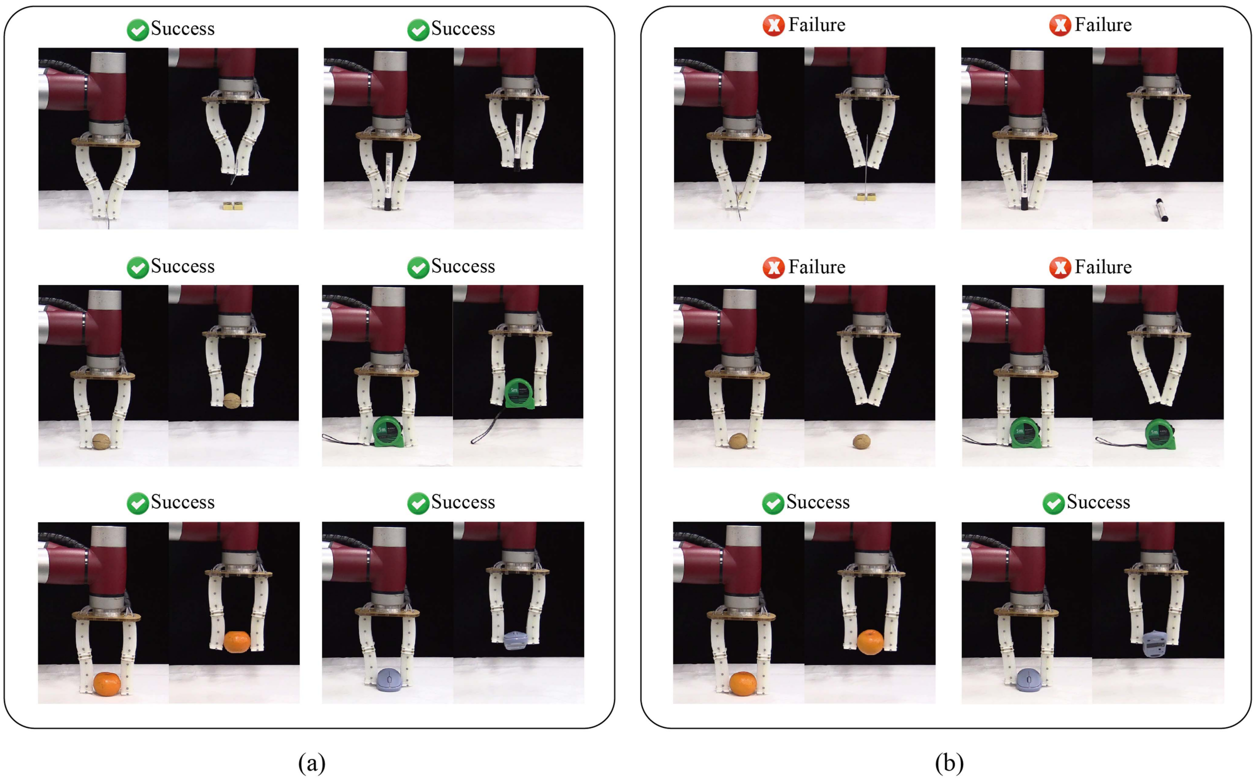

Fig. 11. (a) Parts of the comparative results of grasping tests with the developed adaptive grasping strategy and (b) an open-loop strategy based on proximal segment actuation.

as possible. For this purpose, we apply the following control strategy:

$$\dot{\mathbf{P}} = \mathbf{J}_c{}^{-1}\left[\mathbf{u}_1{}^T \quad -u_2 \mathrm{sign}\left(\theta\right)\right]^T \tag{51}$$

where u_2 is a constant representing the angular velocity that adjusting θ to zero. In addition, $\mathbf{u}_1 = [u_1 \quad 0 \quad 0]^T$ drives $\mathbf{p}_c$ tending to the centerline of the gripper with the velocity of u_1, which contributes to larger contact force. When one or more elements of $\mathbf{P}$ approach their upper limits, the control strategy is switched to

$$\dot{\mathbf{P}} = \mathbf{J}_c{}^{-1}\left[\mathbf{0} \quad -u_2 \mathrm{sign}\left(\theta\right)\right]^T. \tag{52}$$

Implementing (52) until θ is near zero, then the actuation pressures $\mathbf{P}$ will be hold on. Here, the values of u_1, u_2 and the control frequency f_c are set as 30 mm/s, $\pi/24$ rad/s, and 20 Hz, respectively.

To validate our approach, we applied the grasp strategy to nine objects with varying sizes and shapes, as shown in Fig. 10(c). As two cases, photo sequences in Fig. 10(d) illustrate the successful pinch grasp of a nut and a ruler by the gripper, indicating the abilities of the developed strategy in controlling the finger poses during contact, while Fig. 10(e) depicts the evolution of the applied actuation torques throughout the grasping process. In addition, our strategy achieves a 100% success rate (with five repetitions) in all grasping tests for the nine objects. For benchmarking, we included a well-studied open-loop pinch grasp strategy based on proximal-segment actuation [53]. The actions in this strategy are predetermined without the virtual payload introduced in this work as the feedback. Comparative results of the success rates summarized in Table I indicate the effectiveness of our model-based control strategy, and a demonstration video is provided in supplemental Movie S4. As seen in parts of comparative pictures during the grasping tests (see Fig. 11), the control strategy developed in this work can adjust the motions of soft robots autonomously during contact, which enhances the grasping performance.

VII. CONCLUSION AND DISCUSSION

In this study, we report a physics-based modeling and control framework for soft robots operating in uncertain working conditions, such as random payloads, unstructured environments, and uncertain interacting objects. In this framework, utilizing a physical model where both the continuum motions and distributed forces are well parameterized, we construct both a motion-force multimodal estimator and versatile model-based control strategies. The developed estimator can be employed to calculate the complete kinematic configuration of the soft robot and external forces purely using sparse motion sensory units. Experimental results demonstrate the real-time efficiency of the estimator algorithm in updating the parameters of the model-based controller, enabling precise control across arbitrary payload conditions. Remarkably, with the introduction of virtual payloads, our control strategy exhibits robustness even in the presence of model inaccuracy. The average trajectory tracking error is 0.2–0.3 mm with the used experimental setup.

The estimation of external forces empowers soft robots with an understanding of their surrounding environment, including uncertain obstacles and interacting objects, enabling them to adapt accordingly. This versatility makes our control framework suitable for various applications. For example, by leveraging the obstacle positioning method based on the multimodal estimator, we achieve automatic obstacle avoidance for soft manipulators. In addition, we implement an adaptive grasp strategy with contact estimation for a soft gripper, which exhibits significantly improved reliability compared to existing methods. These results highlight the enhanced robustness of the soft robotic system enabled by our proposed estimation and control strategies.

Despite the promising results achieved in this study, there are still several aspects that can be further improved. First, the reliance on an external camera system for the estimator may pose limitations in confined spaces or certain application scenarios. In the future work, the combination with other embedded sensing techniques like inertial measurement units and strain sensors could be explored as an alternative solution. Second, as a first step to achieve precise control of soft robot undergoing uncertain payloads and contacts, this study primarily focuses on low-speed conditions. To enhance its applicability in wider dynamic scenarios, we hope to generalize the control strategy by extending the utilized quasi-static model to a dynamic one and applying more advanced adaptation mechanism in the future work. Third, the virtual payload induced by model inaccuracy exhibits variations across the entire workspace of the robot. To achieve more accurate estimation of the real external forces, data-driven methods such as machine learning could be utilized to extract the virtual payload from the overall estimated forces. Finally, the maximum handling mass of the used gripper is approximately 400 g, limiting its ability to pick up heavier objects. Future work could integrate our proposed strategy with soft grippers featuring variable-stiffness mechanisms [54], [55] to enhance both force capacity and precision.

REFERENCES

[1] D. Rus and M. T. Tolley, "Design, fabrication and control of soft robots," *Nature*, vol. 521, no. 7553, pp. 467–75, 2015.

[2] C. Laschi, B. Mazzolai, and M. Cianchetti, "Soft robotics: Technologies and systems pushing the boundaries of robot abilities," *Sci. Robot*, vol. 1, no. 1, 2016, Art. no. eaah3690.

[3] C. Lee et al., "Soft robot review," *Int. J. Control, Autom. Syst.*, vol. 15, no. 1, pp. 3–15, 2017.

[4] M. Cianchetti, C. Laschi, A. Menciassi, and P. Dario, "Biomedical applications of soft robotics," *Nature Rev. Mater.*, vol. 3, no. 6, pp. 143–153, 2018.

[5] C.-Y. Chu and R. M. Patterson, "Soft robotic devices for hand rehabilitation and assistance: A narrative review," *J. NeuroEng. Rehabil.*, vol. 15, no. 1, 2018, Art. no. 9.

[6] Y. Zhang and M. Lu, "A review of recent advancements in soft and flexible robots for medical applications," *Int. J. Med. Robot. Comput. Assist. Surg.*, vol. 16, no. 3, 2020, Art. no. e2096.

[7] L. Zhou, L. Ren, Y. Chen, S. Niu, Z. Han, and L. Ren, "Bio-inspired soft grippers based on impactive gripping," *Adv. Sci.*, vol. 8, no. 9, 2021, Art. no. 2002017.

[8] C. Tawk, A. Gillett, M. I. H. Panhuis, G. M. Spinks, and G. Alici, "A 3D-printed omni-purpose soft gripper," *IEEE Trans. Robot.*, vol. 35, no. 5, pp. 1268–1275, Oct. 2019.

[9] J. Shintake, V. Cacucciolo, D. Floreano, and H. Shea, "Soft robotic grippers," *Adv. Mater.*, vol. 30, no. 29, 2018, Art. no. 1707035.

[10] R. K. Katzschmann, J. DelPreto, R. MacCurdy, and D. Rus, "Exploration of underwater life with an acoustically controlled soft robotic fish," *Sci. Robot.*, vol. 3, no. 16, 2018, Art. no. eaar3449.

[11] E. W. Hawkes, L. H. Blumenschein, J. D. Greer, and A. M. Okamura, "A soft robot that navigates its environment through growth," *Sci. Robot.*, vol. 2, no. 8, 2017, Art. no. eaan3028.

[12] D. Trivedi, A. Lotfi, and C. D. Rahn, "Geometrically exact models for soft robotic manipulators," *IEEE Trans. Robot.*, vol. 24, no. 4, pp. 773–780, Aug. 2008.

[13] D. C. Rucker and R. J. Webster III, "Statics and dynamics of continuum robots with general tendon routing and external loading," *IEEE Trans. Robot.*, vol. 27, no. 6, pp. 1033–1044, Dec. 2011.

[14] K. M. de Payrebrune and O. M. O'Reilly, "On the development of rod-based models for pneumatically actuated soft robot arms: A five-parameter constitutive relation," *Int. J. Solids Structures*, vol. 120, pp. 226–235, 2017.

[15] K. M. de Payrebrune and O. M. O'Reilly, "On constitutive relations for a rod-based model of a pneu-net bending actuator," *Extreme Mechanics Lett.*, vol. 8, pp. 38–46, 2016.

[16] M. S. Xavier, A. J. Fleming, and Y. K. Yong, "Finite element modeling of soft fluidic actuators: Overview and recent developments," *Adv. Intell. Syst.*, vol. 3, no. 2, 2021, Art. no. 2000187.

[17] P. Ferrentino, E. Roels, J. Brancart, S. Terryn, G. Van Assche, and B. Vanderborght, "Finite element analysis-based soft robotic modeling: Simulating a soft actuator in SOFA," *IEEE Robot. Autom. Mag.*, early access, Mar. 23, 2023, doi: 10.1109/MRA.2022.3220536.

[18] M. A. Graule, T. P. McCarthy, C. B. Teeple, J. Werfel, and R. J. Wood, "SoMoGym: A toolkit for developing and evaluating controllers and reinforcement learning algorithms for soft robots," *IEEE Robot. Autom. Lett.*, vol. 7, no. 2, pp. 4071–4078, Apr. 2022.

[19] S. Tonkens, J. Lorenzetti, and M. Pavone, "Soft robot optimal control via reduced order finite element models," in *Proc. IEEE Int. Conf. Robot. Autom.*, 2021, pp. 12010–12016.

[20] I. S. Godage, R. Wirz, I. D. Walker, and R. J. Webster, "Accurate and efficient dynamics for variable-length continuum arms: A center of gravity approach," *Soft Robot.*, vol. 2, no. 3, pp. 96–106, 2015.

[21] R. K. Katzschmann, C. D. Santina, Y. Toshimitsu, A. Bicchi, and D. Rus, "Dynamic motion control of multi-segment soft robots using piecewise constant curvature matched with an augmented rigid body model," in *Proc. IEEE 2nd Int. Conf. Soft Robot.*, 2019, pp. 454–461.

[22] T. G. Thuruthel, E. Falotico, F. Renda, and C. Laschi, "Model-based reinforcement learning for closed-loop dynamic control of soft robotic manipulators," *IEEE Trans. Robot.*, vol. 35, no. 1, pp. 124–134, Feb. 2019.

[23] A. Tariverdi et al., "A recurrent neural-network-based real-time dynamic model for soft continuum manipulators," *Front. Robot. AI*, vol. 8, 2021, Art. no. 631303.

[24] D. Bruder, X. Fu, R. B. Gillespie, C. D. Remy, and R. Vasudevan, "Data-driven control of soft robots using Koopman operator theory," *IEEE Trans. Robot.*, vol. 37, no. 3, pp. 948–961, Jun. 2021.

[25] D. Bruder, C. D. Remy, and R. Vasudevan, "Nonlinear system identification of soft robot dynamics using Koopman operator theory," in *Proc. Int. Conf. Robot. Autom.*, 2019, pp. 6244–6250.

[26] A. P. Sabelhaus and C. Majidi, "Gaussian process dynamics models for soft robots with shape memory actuators," in *Proc. IEEE 4th Int. Conf. Soft Robot.*, 2021, pp. 191–198.

[27] M. T. Gillespie, C. M. Best, E. C. Townsend, D. Wingate, and M. D. Killpack, "Learning nonlinear dynamic models of soft robots for model predictive control with neural networks," in *Proc. IEEE Int. Conf. Soft Robot.*, 2018, pp. 39–45.

[28] M. Azizkhani, I. S. Godage, and Y. Chen, “Dynamic control of soft robotic arm: A simulation study,” *IEEE Robot. Autom. Lett.*, vol. 7, no. 2, pp. 3584–3591, Apr. 2022.

[29] M. Azizkhani, A. L. Gunderman, I. S. Godage, and Y. Chen, “Dynamic control of soft robotic arm: An experimental study,” *IEEE Robot. Autom. Lett.*, vol. 8, no. 4, pp. 1897–1904, Apr. 2023.

[30] M. S. Xavier, A. J. Fleming, and Y. K. Yong, “Nonlinear estimation and control of bending soft pneumatic actuators using feedback linearization and UKF,” *IEEE/ASME Trans. Mechatron.*, vol. 27, no. 4, pp. 1919–1927, Aug. 2022.

[31] A. Centurelli, L. Arleo, A. Rizzo, S. Tolu, C. Laschi, and E. Falotico, “Closed-loop dynamic control of a soft manipulator using deep reinforcement learning,” *IEEE Robot. Autom. Lett.*, vol. 7, no. 2, pp. 4741–4748, Apr. 2022.

[32] G. Fang et al., “Vision-based online learning kinematic control for soft robots using local Gaussian process regression,” *IEEE Robot. Autom. Lett.*, vol. 4, no. 2, pp. 1194–1201, Apr. 2019.

[33] J. Lai, B. Lu, and H. K. Chu, “Variable-stiffness control of a dual-segment soft robot using depth vision,” *IEEE/ASME Trans. Mechatron.*, vol. 27, no. 2, pp. 1034–1045, Apr. 2022.

[34] Z. Shen et al., “High-stretchability, ultralow-hysteresis conducting polymer hydrogel strain sensors for soft machines,” *Adv. Mater.*, vol. 34, no. 32, 2022, Art. no. 2203650.

[35] P. Karipoth, A. Christou, A. Pullanchiyodan, and R. Dahiya, “Bioinspired inchworm- and earthworm-like soft robots with intrinsic strain sensing,” *Adv. Intell. Syst.*, vol. 4, no. 2, 2022, Art. no. 2100092.

[36] K. C. Galloway, Y. Chen, E. Templeton, B. Rife, I. S. Godage, and E. J. Barth, “Fiber optic shape sensing for soft robotics,” *Soft Robot.*, vol. 6, no. 5, pp. 671–684, 2019.

[37] R. A. Bilodeau, E. L. White, and R. K. Kramer, “Monolithic fabrication of sensors and actuators in a soft robotic gripper,” in *Proc. IEEE/RSJ Int. Conf. Intell. Robots Syst.*, 2015, pp. 2324–2329.

[38] L.-Y. Zhou, Q. Gao, J.-F. Zhan, C.-Q. Xie, J.-Z. Fu, and Y. He, “Three-dimensional printed wearable sensors with liquid metals for detecting the pose of snake like soft robots,” *ACS Appl. Mater. Interfaces*, vol. 10, no. 27, pp. 23208–23217, 2018.

[39] O. Shorthose, A. Albini, L. He, and P. Maiolino, “Design of a 3D-printed soft robotic hand with integrated distributed tactile sensing,” *IEEE Robot. Autom. Lett.*, vol. 7, no. 2, pp. 3945–3952, Apr. 2022.

[40] R. L. Truby et al., “Soft somatosensitive actuators via embedded 3D printing,” *Adv. Mater.*, vol. 30, no. 15, 2018, Art. no. 1706383.

[41] B. Ward-Cherrier et al., “The TacTip family: Soft optical tactile sensors with 3D-printed biomimetic morphologies,” *Soft Robot.*, vol. 5, no. 2, pp. 216–227, 2018.

[42] T. G. Thuruthel, B. Shih, C. Laschi, and M. T. Tolley, “Soft robot perception using embedded soft sensors and recurrent neural networks,” *Sci. Robot.*, vol. 4, no. 26, 2019, Art. no. eaav1488.

[43] Y. Chen, L. Wang, K. Galloway, I. Godage, N. Simaan, and E. Barth, “Modal-based kinematics and contact detection of soft robots,” *Soft Robot.*, vol. 8, no. 3, pp. 298–309, 2020.

[44] Z. Zhang, J. Dequidt, and C. Duriez, “Vision-based sensing of external forces acting on soft robots using finite element method,” *IEEE Robot. Autom. Lett.*, vol. 3, no. 3, pp. 1529–1536, Jul. 2018.

[45] C. D. Santina, R. L. Truby, and D. Rus, “Data-driven disturbance observers for estimating external forces on soft robots,” *IEEE Robot. Autom. Lett.*, vol. 5, no. 4, pp. 5717–5724, Oct. 2020.

[46] A. A. Shabana and R. Y. Yakoub, “Three dimensional absolute nodal coordinate formulation for beam elements: Theory,” *J. Mech. Des.*, vol. 123, no. 4, pp. 606–613, 2000.

[47] A. A. Shabana and A. E. Eldeeb, “Motion and shape control of soft robots and materials,” *Nonlinear Dyn.*, vol. 104, pp. 165–189, 2021.

[48] X. Huang, X. Zhu, and G. Gu, “Kinematic modeling and characterization of soft parallel robots,” *IEEE Trans. Robot.*, vol. 38, no. 6, pp. 3792–3806, Dec. 2022.

[49] X. Huang, J. Zou, and G. Gu, “Kinematic modeling and control of variable curvature soft continuum robots,” *IEEE/ASME Trans. Mechatron.*, vol. 26, no. 6, pp. 3175–3185, Dec. 2021.

[50] Y. C. Fung and P. Tong, *Classical and Computational Solid Mechanics*. Singapore: World Scientific, 2001.

[51] E. K. Chong and S. H. Żak, *An Introduction to Optimization*. Hoboken, NJ, USA: Wiley, 2013.

[52] H. Choset, K. M. Lynch, S. Hutchinson, G. A. Kantor, and W. Burgard, *Principles of Robot Motion: Theory, Algorithms, and Implementations*. Cambridge, MA, USA: MIT press, 2005.

[53] C. B. Teeple, T. N. Koutros, M. A. Graule, and R. J. Wood, “Multi-segment soft robotic fingers enable robust precision grasping,” *Int. J. Robot. Res.*, vol. 39, no. 14, pp. 1647–1667, 2020.

[54] Y. Zhao et al., “A soft continuum robot, with a large variable-stiffness range, based on jamming,” *Bioinspiration Biomimetics*, vol. 14, Sep. 2019, Art. no. 066007.

[55] S. Jadhav, M. R. A. Majit, B. Shih, J. P. Schulze, and M. T. Tolley, “Variable stiffness devices using fiber jamming for application in soft robotics and wearable haptics,” *Soft Robot.*, vol. 9, no. 1, pp. 173–186, 2022.

Xinjia Huang received the B.E. degree (Honors.) in engineering mechanics from Chongqing University, Chongqing, China, in 2018. He is currently working toward the Ph.D. degree in mechanical engineering with Shanghai Jiao Tong University, Shanghai, China.

His research interests include design, modeling, and control of soft robotics.

Zihao Yuan received the B.E. degree in mechanical engineering from Shanghai Jiao Tong University, Shanghai, China, in 2022, where he is currently working toward the M.S. degree in mechanical engineering.

His research interests include design and control of pneumatic soft robots, and bioinspired soft robots.

Xinyu Yang received the B.E. degree in mechanical engineering from Shanghai Jiao Tong University, Shanghai, China, in 2021, where he is currently working toward the Ph.D. degree in mechanical engineering.

His research interests include design and control of soft anthropomorphic hand and variable stiffness technology of soft actuators.

Guoying Gu (Senior Member, IEEE) received the B.E. degree (Hons.) in electronic science and technology, and the Ph.D. degree (Hons.) in mechatronic engineering from Shanghai Jiao Tong University, Shanghai, China, in 2006 and 2012, respectively.

He is currently a Distinguished Professor with the School of Mechanical Engineering, Shanghai Jiao Tong University. He was a Humboldt Fellow with University of Oldenburg, Germany. He was a Visiting Scholar with Massachusetts Institute of Technology, National University of Singapore and Concordia University. His research interests include soft robotics, bioinspired and wearable robots, smart materials sensing, actuation and motion control. He is the author or coauthor of over 100 publications, which have appeared in *Science Robotics*, *Nature Biomedical Engineering*, *Nature Reviews Materials*, *Nature Materials, Nature Communications, Science Advances*, IEEE/ASME TRANSACTIONS, Advanced Materials, Soft Robotics, Science China serials etc., as book chapters and in conference proceedings. He has also served for several journals as Editorial Board Member, Topic Editor, or Guest Editor, and several international conferences/symposiums as Chair, Co-Chair, an Associate Editor or Program Committee Member.

Dr. Gu received the National Science Fund for Distinguished Young Scholars and the XPLORER PRIZE. He was an Associate Editor of Soft Robotics. He was an Associate Editor of IEEE TRANSACTIONS ON ROBOTICS and IEEE ROBOTICS AND AUTOMATION LETTERS.